# Prevalent glacial North Atlantic Deep Water despite Arctic freshwater input

Patrick Blaser [1,2]*

Jörg Lippold [2]

Claire Waelbroeck [3]

David J. Thornalley [4]

Frerk Pöppelmeier [5,6]

Stefanie Kaboth-Bahr [7]

Janne Repschläger [8]

Samuel L. Jaccard [1,6]

[1] Institute of Earth Sciences, University of Lausanne, Lausanne, Switzerland

[2] Institute of Earth Sciences, Heidelberg University, Heidelberg, Germany

[3] LOCEAN/IPSL, Sorbonne Université-CNRS-IRD-MNHN, UMR7159, Paris, France

[4] Department of Geography, University College London, UK

[5] Climate and Environmental Physics, Physics Institute, University of Bern, Bern, Switzerland

[6] Oeschger Centre for Climate Change Research, University of Bern, Bern, Switzerland

[7] Institute for Geosciences, University of Potsdam, Karl-Liebknecht-Straße 24-26, Potsdam, Germany

[8] Department of Climate Geochemistry, Max-Planck Institute for Chemistry, Mainz, Germany

* corresponding author

# Abstract

Changes in the configuration and properties of deep ocean water masses modulated Quaternary climate transitions between ice ages and interglacials. For example, it is thought that North Atlantic Deep Water (NADW) was volumetrically reduced during the last glacial period. Yet, reconstructions based on individual types of proxy observations yield diverging results about the past spatial extent and properties of NADW.

Here we combine observations from five different proxies for the reconstruction of Atlantic source water distributions during the Last Glacial Maximum and Heinrich Stadial 1 (23.0 – 14.6 thousand years before present). We find evidence that NADW prevailed in a similar manner as today, albeit both upper and lower NADW existed in two distinct source water modes each, one cold and well ventilated and another less ventilated and possibly warmer.

The inclusion of all four glacial NADW components in estimations of Atlantic deep water provenance suggest that NADW was prevalent during both time periods, even though significant freshwater fluxes presumably perturbed NADW formation during Heinrich Stadial 1. We hence suggest that NADW during the last glacial was surprisingly prevalent and resilient to disturbance on millennial time scales, which is important for our understanding of the Atlantic overturning circulation.

## ---------- Main ----------

Ocean circulation modulates the meridional distribution of heat and marine carbon storage and thus plays a crucial role in global climate on decadal to geological time scales (Stocker, 2013). Observations from past climates characterised by a range of different boundary conditions provide a benchmark to critically assess our understanding of the climate system and the robustness of global climate models.

Reconstructions of past changes in deep water sourcing can be used to constrain ocean dynamics. Yet, available paleoceanographic reconstructions appear conflicting, even for arguably well documented climate intervals including the Last Glacial Maximum (LGM, ~ 23 - 19 thousand years before present, ka BP) and Heinrich Stadial 1 (HS1, 17.5 - 14.6 ka BP; Waelbroeck et al., 2019). Solving inconsistencies in reconstructions of past deep water sourcing and hence ocean circulation would yield important insights into climate - ocean relationships.

The modern Atlantic deep water geometry can be accurately deconvolved using oceanographic properties such as temperature, salinity, and nutrient contents (de Carvalho Ferreira and Kerr, 2017). It shows that North Atlantic Deep Water (NADW) fills most of the Atlantic Ocean before it leaves to the south and feeds into the Antarctic Circumpolar Current and the production of Antarctic Bottom Water (AABW; Johnson, 2008; Marshall and Speer, 2012). In contrast, the abyssal South Atlantic basins are bathed by less ventilated and dense AABW, which penetrates northwards, yet contributes less than 25 % to the water mass mixture in the deepest Northwest Atlantic (de Carvalho Ferreira and Kerr, 2017). Essentially, these two main deep waters connect the oxygen, carbon, and heat budgets of the deep ocean to the atmosphere.

NADW is composed of two distinct source water types produced through buoyancy loss at high latitudes (Petit et al., 2020). Dense water formed in the Arctic Mediterranean (AMW) overflows the sills around Iceland into the deep North Atlantic. During its descent AMW entrains subsurface water and upper NADW (u-NADW, alternatively referred to as Labrador Sea Water), which itself is produced in the subpolar North Atlantic (Fig. 1). The overflow waters thereby roughly double their volume flux and form lower NADW (l-NADW; Bower et al., 2019; Dickson and Brown, 1994; Price and O'Neil Baringer, 1994).

Initial paleoceanographic reconstructions have indicated that NADW was much shallower and less vigorous during the LGM (Curry et al., 1988; Lynch-Stieglitz, 2017; McManus et al., 2004). Although more recent studies challenged many of these findings (Blaser et al., 2020; Hines et al., 2021; Howe et al., 2016; Keigwin and Swift, 2017; Oppo et al., 2018; Pöppelmeier et al., 2020; Seidenkrantz et al., 2021; Skinner et al., 2021), the paradigm still prevails that the production of Atlantic northern sourced waters was substantially weaker during the last glacial than during the Holocene and its prevalence accordingly reduced. In consequence, less ventilated AABW and Pacific Deep Water (PDW; Yu et al., 2020) were more voluminous, which supposedly allowed for a stronger sequestration of carbon from the atmosphere. Equally, there was an increased potential for $CO_2$ release in the course of water mass reorganisation during the following deglaciation, modulating the timing and pace of climate change (Skinner et al., 2021).

Heinrich Stadial 1 occurred at the end of the last glacial and was marked by widespread ice berg discharge into the North Atlantic, leading to fresh water input which supposedly disturbed the

buoyancy balance and limited the potential for deep convection (Marcott et al., 2011). It is thought that the AMOC thus weakened substantially and less heat was transported northward, leading to pronounced northern hemisphere cooling. However, the strength of NADW and AABW production under these conditions and the associated water mass configuration remain even more debated than for the LGM (Bradtmiller et al., 2014; Evans and Hall, 2008; Labeyrie et al., 2005; Lippold et al., 2012; Ng et al., 2018; Repschläger et al., 2021; Süfke et al., 2019; Waelbroeck et al., 2011)

Importantly, many inconsistencies in these reconstructions remain (see citations above). Hence, even though they are critical components of the climate system and the LGM and HS1 are two relatively well constrained climate intervals, the past properties, volume flux, and distribution of NADW remain largely uncertain.

We argue that a large part of this inconsistency is owed to the fact that paleoceanographic reconstructions must rely on indirect proxy analyses, which bear significant uncertainties and potential for biases. Importantly, proxy signatures in seawater can be affected by other processes than passive advection, and geochemical proxy archives can be altered by diagenetic processes. Higher confidence is achieved when observations from independent proxies and across different regions are combined.

In this context, we discuss evidence for diverse intermediate and deep water properties in the source region of NADW, and subsequently assimilate new and published data from five proxies across the deep Atlantic with an isotope mixing model in order to constrain a consistent multi-proxy picture of the Atlantic deep circulation geometry during two distinct phases of the last glacial period, namely the LGM and HS1.

## Northern source waters during the late glacial

High stable isotope signatures in the calcite shells of benthic organisms ($\delta^{13}C_b$ & $\delta^{18}O_b$, see Methods) evidence the presence of cold and well ventilated glacial u-NADW in the intermediate depth (here between 1.0 and 2.5 km water depth) Iceland Basin during the last glacial period (Fig. 1). At the same time, stable isotope signatures at greater depth, in the intermediate depth Arctic Mediterranean, and in the western subpolar North Atlantic exhibited lower $\delta^{13}C_b$ and in part also lower $\delta^{18}O_b$ signatures. During HS1, the trend to lower $\delta^{13}C_b$ and $\delta^{18}O_b$ became greater and encompassed the entire region including the intermediate depth Iceland Basin. In the Iceland Basin, this apparent loss of u-NADW signatures during HS1 has been suggested to derive from a combination of changes in the isotopic composition of the source waters and in particular an increased admixture of SSW (Oppo et al., 2015). However, εNd-based and combined $\delta^{13}C_b$ - $\delta^{18}O_b$ observations suggest that SSW was never dominant in the Northwest Atlantic water mass mixture during the LGM or HS1 (Blaser et al., 2020; Gutjahr et al., 2010; Pöppelmeier et al., 2020, 2018; Repschläger et al., 2021; Zhao et al., 2019). In light of these reconstructions, we reassess the properties of glacial North Atlantic source waters, with a focus on stable isotope compositions (Meland et al., 2008; Millo et al., 2006; Oppo et al., 2015; Thornalley et al., 2010), as they are the most established and abundant reconstructions in this region and are usually available as proxy pairs due to their combined measurement (see Methods for details).

Across the intermediate depth Arctic Mediterranean and Iceland Basin, as well as intermediate to deep Irminger and Labrador seas, glacial stable isotope data span a quadrangle ranging roughly from 0 to 1.7 ‰ in $\delta^{13}C_b$ and 1.7 to 4.0 ‰ in $\delta^{18}O_{b,ivoc}$ space (ivoc: ice-volume and core-top offset

corrected; see Methods and Fig. 1). We hypothesise that these four corners relate to distinct source waters whose mixing produced water masses with the archived isotopic signatures. Data that are both high in $\delta^{13}C_b$ and $\delta^{18}O_{b,ivoc}$ were most prevalent at intermediate depths in the Iceland Basin and Irminger Sea and correspond to the canonical glacial u-NADW. At lower $\delta^{13}C_b$ and slightly higher $\delta^{18}O_{b,ivoc}$ we identify another source water most prevalent in the Arctic Mediterranean, followed by the western subpolar North Atlantic, and which we accordingly refer to as glacial AMW. Since AMW appears to have occupied depths below u-NADW, it can be regarded as the source water of glacial l-NADW just as today (see Fig. 1 A).

The two last source water signatures are marked by much lower $\delta^{18}O_{b,ivoc}$ and slightly lower $\delta^{13}C_b$ values. The source water with the lowest $\delta^{18}O_{b,ivoc}$ of ~ 2.2 ‰ or less has previously been suggested to have replaced glacial u-NADW during HS1 (Oppo et al., 2015). Its low stable isotope signatures have been interpreted to reflect formation via densification through sea ice brine rejection and entrainment of meteoric water (Dokken and Jansen, 1999; Meland et al., 2008; Thornalley et al., 2010; Waelbroeck et al., 2011), and/or SSW (Oppo et al., 2015). However, this source water could not have been substantially influenced by SSW because its most prominent occurrence clearly lies in the subpolar North Atlantic. Moreover, these subpolar North Atlantic locations do not show any other indications of SSW provenance such as low seawater $[CO_3^{2-}]$ (Yu et al., 2008), and data from these sites define a trend in the stable isotope space that is tangential to deep SSW (AABW & PDW, see Fig. 1). For these reasons, we argue that this source water represents another mode of u-NADW, and hence term these two source water modes as u-NADW-1 and u-NADW-2. Interestingly, data trending towards u-NADW-2 are not restricted to HS1, but are also observed in LGM sediments in particular in the Irminger and Labrador seas, albeit generally to a lesser degree.

Finally, the remaining source water at lowest $\delta^{13}C_b$ of ~ 0 is the least prevalent in the data. The intermediate and deep Irminger and Labrador seas sites trend towards these signatures predomiantly during HS1. These are the same sites as the ones that show signatures close to AMW in LGM sediments. Therefore, and because the trend between these signatures and AMW is similar to the trend between the two modes of u-NADW, we hypothesise this source water to be a second mode of AMW, namely AMW-2.

To summarise, we find that both upper and lower NADW existed during the LGM and HS1 similar to today. Furthermore, each of these two NADW types appears to have existed in two different modes, one with relatively high carbon and oxygen isotope signatures (mode 1) and one with significantly lower isotopic signatures (mode 2).

## Multi-proxy estimate of glacial NADW abundance

Considering the newly defined four components of NADW we investigate the deep Atlantic water mass composition during the LGM, HS1, and the Late Holocene (LH; as a sedimentary equivalent of today). We consider water depths below 2 km and latitudes between ~ 48 °N and 15 °S (Extended Data Fig. 1) and a compilation of five geochemical proxies ($\delta^{13}C_b$, $\delta^{18}O_{b,ivoc}$, the radiogenic isotope composition of neodymium (εNd), the carbonate ion concentration $[CO_3^{2-}]$ inferred from foraminifera B/Ca ratios, and the radiocarbon age of deep waters inferred from foraminifera radiocarbon contents; see Supplementary Text 1 and Supplementary Fig. 2). With the help of observations from the source regions of the respective source waters we estimate the proxy signatures for two SSW (AABW, PDW) and four northern source waters (u-NADW-1, u-NADW-2,

AMW-1, AMW-2 for LGM and HS1, and instead u-NADW and l-NADW for LH; Fig. 2, see also Supplementary Text 2 and Supplementary Tables 3 & 4). Source water signatures and proxy data are then fed into a Bayesian isotope mixing model (Parnell and Inger (2016), see Methods) to calculate source water contributions for proxy observations in the deep Atlantic.

For the mixing calculations we aggregate observations within discrete sub-volumes of the Atlantic (see Methods and Extended Data Fig. 1) and estimate source water contributions best fitting all proxy observations simultaneously within each volume for each time slice. The advantages of this mixing model are (i) the reliance solely on observations and source water signatures without potential over-constraints or biases from model-physics implementations or a priori knowledge about source water formation mechanisms, (ii) the incorporation of an arbitrary number of source waters and proxies, (iii) full integration of source water signature uncertainties, and (iv) computational efficiency. We exploit these advantages by constructing a large ensemble of 3000 model parametrisations reflecting variations in the model systematics, wide ranges in the strengths of non-conservative proxy mechanisms, and the incorporation of different combinations of proxies and source waters (see Methods and Extended Data Table 1).

The estimated contribution of NADW in the deep Atlantic is remarkably invariant across the investigated time periods (Fig. 3). For model solutions employing all source waters, NADW contributions average to 73 ± 14 % for the LGM (median & 95 % range), 74 ± 15 % for HS1, and 76 ± 19 % for the LH, compared to about 82 % today assessed from oceanographic tracers (de Carvalho Ferreira and Kerr, 2017). These high contributions of NADW contrast recent lower estimates for the LGM of 49 and 56 % (Oppo et al., 2018; Pöppelmeier et al., accepted). Agreement with these studies is achieved if NADW is restricted to its classical u-NADW-1 source water type, which reduces the median amount of NADW during the LGM, HS1, and LH by 24, 29 and 12 %, respectively (Fig. 3). This systematic shows the important consequences of including the newly defined NADW source water types in modelling attempts. Notably, the detailed differences between time slices mainly depend on the strength of non-conservative proxy processes, among which the amount of decomposed organic matter has the strongest effect (see Methods and Extended Data Fig. 3).

For the LGM and HS1 both the overall amount of NADW and its distribution agree across most of the model ensemble (Fig. 4, Supplementary Fig. 18), and are clearly at odds with a strong reduction of NADW prevalence in the Atlantic during HS1. This observation calls for active deep water formation in the North Atlantic during HS1 (Labeyrie et al., 2005; Repschläger et al., 2021). The ratio of northern to southern sourced water in the Atlantic should be strongly influenced by both their relative densities and volume fluxes. The lack of a substantial reduction in NADW prevalence from the LGM to HS1 found here thus suggests that neither relative densities nor fluxes changed significantly, or rather changed in the same direction for both northern and southern source waters. For example, a reduction in the volume flux of both NADW and SSW during HS1 would be conceivable, and would agree with evidence for a weakened AMOC during HS1 (Bradtmiller et al., 2014; McManus et al., 2004).

Interestingly, the results suggest that during both LGM and HS1 there was a significantly higher ratio of AMW to u-NADW filling the Atlantic than today (Fig. 3). This observation could indicate less entrainment of shallow and intermediate depth waters into AMW during overflow. Low entrainment in turn can generally be caused by reduced production or lower relative density of AMW (Price and O’Neil Baringer, 1994).

Even though the NADW contributions are inferred to be similar for the LGM and HS1, proxy signatures did change to variable degrees. These shifts can thus be generally explained by changes in the composition of NADW itself and do not require major reorganisations of Atlantic source water provenance. In particular, proxy changes from LGM to HS1 appear to be caused by an increase of mode 2 NADW from 24 ± 13 % to 34 ± 17 % (Fig. 3).

## Mechanisms of glacial NADW formation

Open ocean convection as it occurs around the North Atlantic today leads to efficient ocean-atmosphere coupling, and results in both high $\delta^{18}O_b$ and $\delta^{13}C_b$ signatures at depth. While this is observed for glacial u-NADW-1, the $\delta^{13}C_b$ of AMW-1 is significantly lower (1.20 ± 0.09; Fig. 2). This is particularly important because the existence of a low-$\delta^{13}C_b$ NADW type significantly affects water mass sourcing estimates when based on this widely used proxy. These lower isotopic signatures could have been caused by an increased imprint from organic matter remineralisation from the large Arctic Mediterranean (Ezat et al., 2021) or by reduced air-sea gas exchange owing to more extended sea ice cover. Such a process has also been proposed as a cause for particularly low $\delta^{13}C_b$ values in the Atlantic sector of the Southern Ocean (Mackensen, 2012; Williams et al., 2019).

Our estimated proxy signatures of mode 2 source waters (u-NADW-2 and AMW-2) are characterised by lower $\delta^{13}C_b$ and $\delta^{18}O_b$ values than their mode 1 counterparts, and generally similar εNd (Blaser et al., 2020; Zhao et al., 2019). There is less clear evidence for relatively high radiocarbon ventilation ages (Thornalley et al., 2011), as well as slightly lower [$CO_3^{2-}$] for mode 2 source waters (Fig. 2; Yu et al., 2008). While the similar εNd signatures between mode 1 and mode 2 waters support invariant geographic origins, the disparities in the other proxies indicate considerable differences in their physical and chemical properties.

Traditionally, the observation of low $\delta^{18}O_b$ in the glacial North Atlantic and Nordic Seas has been linked to the incorporation of meteoric (melt)waters with very low $\delta^{18}O$, brought to depth for example by sinking brines from sea ice production (Dokken and Jansen, 1999; Meland et al., 2008; Thornalley et al., 2010). Alternatively, higher temperatures could explain the low $\delta^{18}O_b$ signatures of mode 2 source waters (Fig. 2; El bani Altuna et al., 2021; Marchitto et al., 2014; Marcott et al., 2011). The necessary temperature differences between source water modes would be substantial, with up to 4 and 6 °C for AMW and u-NADW, respectively. It appears unlikely that such warm and still dense waters were generated by open ocean convection, and therefore the mixing with warm and saline subsurface water, for example from the Mediterranean Sea, has been suggested to have acted as the heat source (Labeyrie et al., 2005; Repschläger et al., 2021). Yet, the low $\delta^{13}C_b$ signatures combined with apparently higher radiocarbon ages in the mode 2 source waters still suggest that either surface gas exchange was reduced for these source water modes, probably due to increased sea ice and fresh water cover on the high latitude ocean (Khatiwala et al., 2019; Mackensen, 2012), or they were mixed with a larger and older carbon pool, for example from the Arctic Mediterranean. The exact mechanisms cannot be determined from our findings, but the suggested source water proxy signatures will promote future investigations.

It is noteworthy that the potential for warm mode 2 northern sourced waters is climatically highly relevant. If warm deep waters were actively produced, then this process would relay heat that is advected to the high latitude northern hemisphere into the deep ocean instead of the atmosphere. Transported south from the deep North Atlantic in particular during HS1, this heat would have

warmed the global deep oceans as well as the shallow waters of the Southern Ocean, where it could have promoted Antarctic ice shelf melt.

# Conclusions

Coupled oxygen and carbon stable isotope data from the high latitude North Atlantic indicate that a complex interplay of at least four distinct northern source deep waters existed during the late glacial. They derived from a mixture of upper and lower NADW in a similar fashion as today. We hypothesise that these two water types both existed in well-ventilated open ocean modes (mode 1) as well as in a second mode that was less ventilated and potentially warmer (mode 2). Both modes of both source water types contributed to NADW during the LGM and HS1, with only a moderately higher fraction of mode 2 source waters during HS1.

When all of these source waters are included into mixing calculations the widely proposed differences in NADW prevalence between LGM and HS1 states disappear. Instead, the volume of NADW was likely only moderately less than today, mainly in the deepest North Atlantic. Notably, several independent lines of evidence nonetheless point to less vigorous NADW volume flux during glacial times than today, indicating a weak link between NADW prevalence and AMOC strength.

The similarity of NADW distribution between LGM and HS1 in spite of northern hemisphere cooling and large upper North Atlantic stratification changes during HS1 with respect to the LGM indicate that mode 2 deep water formation compensated the decrease of open ocean (mode 1) deep water formation in the North Atlantic. This formation of less ventilated and potentially warm deep water could have occurred by sea ice brine formation and/or subsurface mixing with warm and salty water. The source water properties suggest a weaker link of these mode 2 source waters to the atmosphere, in line with a regionally stronger ice cover and stratification. Similar shifts in deep water formation may have occurred during earlier stadial intervals including Heinrich Stadials and Dansgaard-Oeschger Stadials. We hence suggest that changes in ocean-atmosphere exchange and deep water formation mode in the glacial Arctic and North Atlantic are crucial to understand past ocean circulation and ocean-climate interaction. Our results show that the glacial Atlantic deep water mass geometry was more resilient to changes than previously thought, even though deep water properties and high latitude freshwater fluxes evidently changed.

# Acknowledgements

Sediment material was provided by the ODP/IODP core repository in Bremen, Germany. PB acknowledges fundings from the Deutsche Forschungsgemeinschaft (grant LI1815/4), the Bundesagentur für Arbeit during unemployment, and the Swiss National Science Foundation (grant 192361 awarded to SLJ). CW acknowledges support from the European Research Council (ERC grant ACCLIMATE/n° 339108). FP received funding from the European Union's Horizon 2020 research and innovation program (grant agreements No 101023443, project CliMoTran). SKB acknowledges funding from ECORD Young Scientist Grant as well as an Open-Top Post-Doc fellowship of the University of Potsdam. Data analysis has been performed with the *R* software including several published packages such as *tidyverse* collection.

# Figures

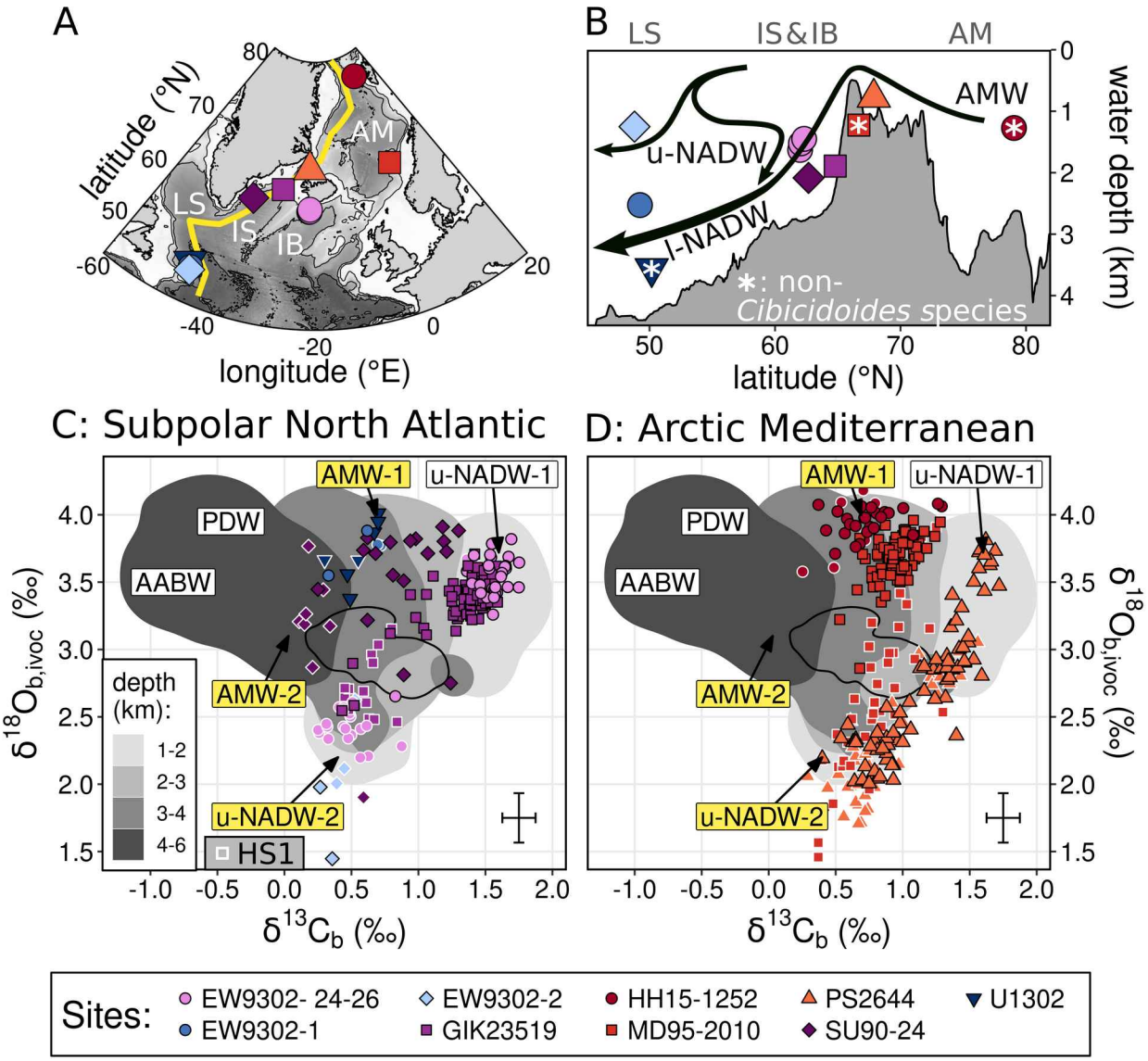


***Fig. 1:*** *Benthic stable isotope data from across the subpolar North Atlantic and Arctic Mediterranean (AM).* ***A:*** *Map with selected sediment core sites used in C and D. Selected sites feature high resolution data and cover different regions of young northern sourced water with less than 5% SSW today (de Carvalho Ferreira and Kerr, 2017). LS: Labrador Sea, IS: Irminger Sea, IB: Iceland Basin.* ***B:*** *Section along yellow line in A with sediment sites projected on. Arrows indicate modern NADW tributary water flows (see text).* ***C & D****: Stable isotope spaces of late glacial data (23 – 14.6 ka BP; white borders indicate HS1 age). Areas in background indicate compiled West Atlantic data in grey according to their water depths. Black outline marks full data distribution in modern Atlantic seawater from > 2 km depth. Labels indicate isotopic signatures of different glacial source waters, with the ones suggested in this study marked yellow. Data from non-*Cibicides *species (see B) were corrected for species-specific offsets (see Methods). All* $\delta^{18}O$ *data are corrected for continental ice volume (ivc) changes and where possible for core top-seawater offset (oc, see Methods). Error crosses in C & D indicate typical double standard deviation uncertainties including those from ivc. See Supplement for data sources.*

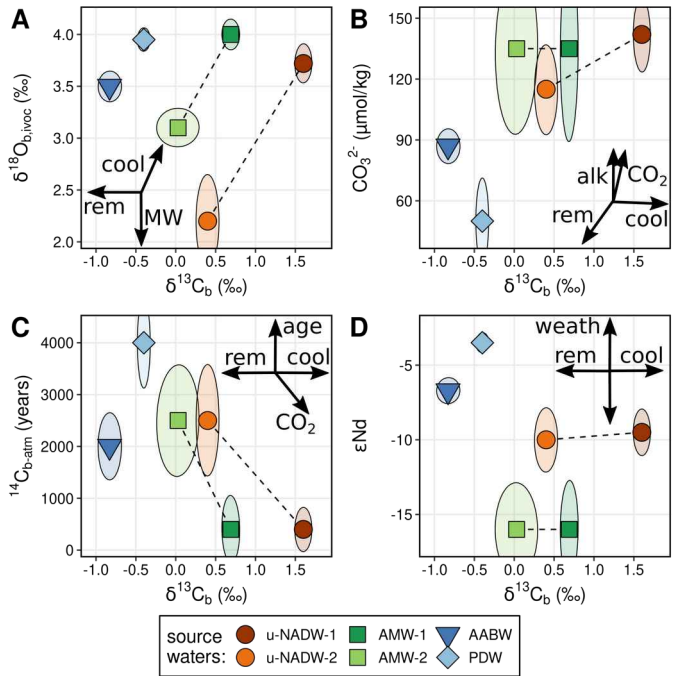


296

***Fig. 2:*** *Glacial Atlantic source water signatures in proxy-proxy spaces. Different source waters are shown as coloured symbols, and estimated 95% level uncertainties as error ellipses. Dashed lines connect different source water modes of the same source water type (u-NADW and AMW). Arrows indicate processes that can affect source water proxy signatures:* ***cool:*** *surface water cooling;* ***rem:*** *organic matter remineralsation;* ***MW:*** *meteoric water admixture;* ***alk:*** *alkalinity increase;* ***$CO_2$:*** *$CO_2$ evasion (slope depends on dynamics);* ***age:*** *carbon ventilation age increase,* ***weath:*** *input of Nd through weathering. See Extended Data Fig. 2 for source water signatures today.*

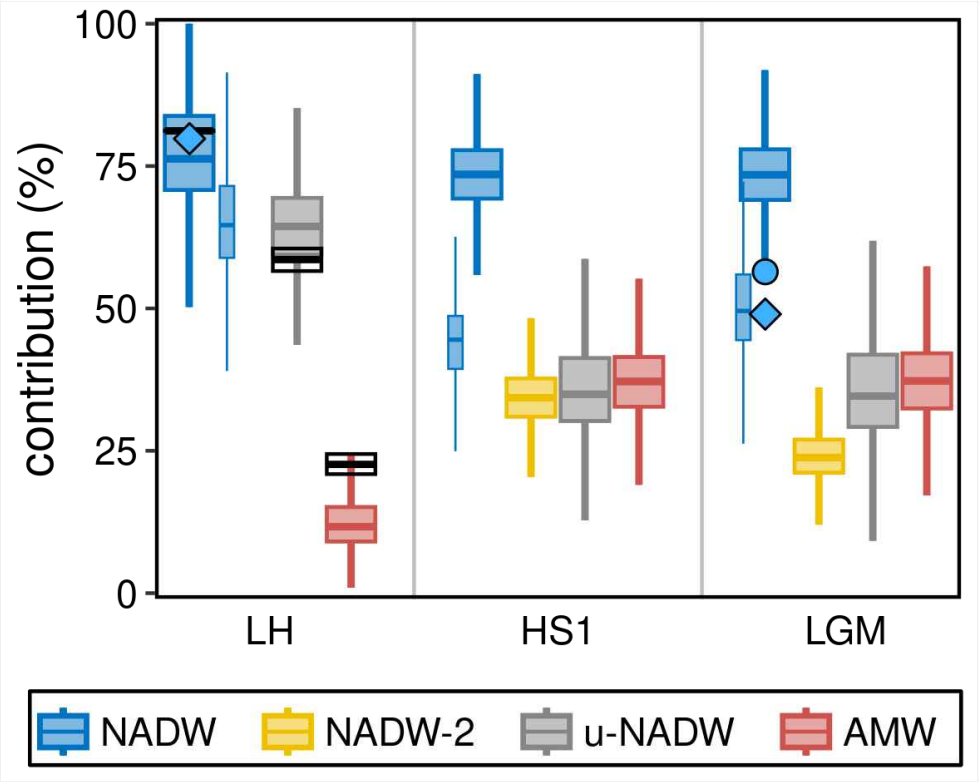


297

***Fig. 3:*** *Mixing model ensemble results for average NADW contributions. Results are shown as boxes spanning 50% of data and including median lines, as well as whiskers spanning 95% data ranges. Colours indicate different NADW types and modes for each time slice (NADW-2 = u-NADW-2 + l-NADW-2). The thin blue NADW boxes are results from a sub-ensemble where the suggested new source waters are excluded (i.e. NADW:= u-NADW-1; 357 runs; exclusion of AMW and of mode 2 source waters contributing similarly for the glacial time slices, see also Extended Data Fig. 3). Black horizontal bars at Late Holocene (LH) are mean values from analyses of oceanographic tracers in actual seawater (de Carvalho Ferreira and Kerr, 2017). Blue diamonds are results from Bern3D intermediate complexity Earth System model* (Pöppelmeier et al., 2022, accepted) *and blue circle at LGM shows results from (Oppo et al., 2018). All data are from the Atlantic below 2 km water depth and latitudes between ~ 48 °N and 15 °S. For the LH, u-NADW and l-NADW contributions were originally estimated, and were converted to u-NADW and AMW by assuming 55 ± 5 % fractional entrainment in l-NADW for better comparison (Dickson and Brown, 1994).*

298

299

300

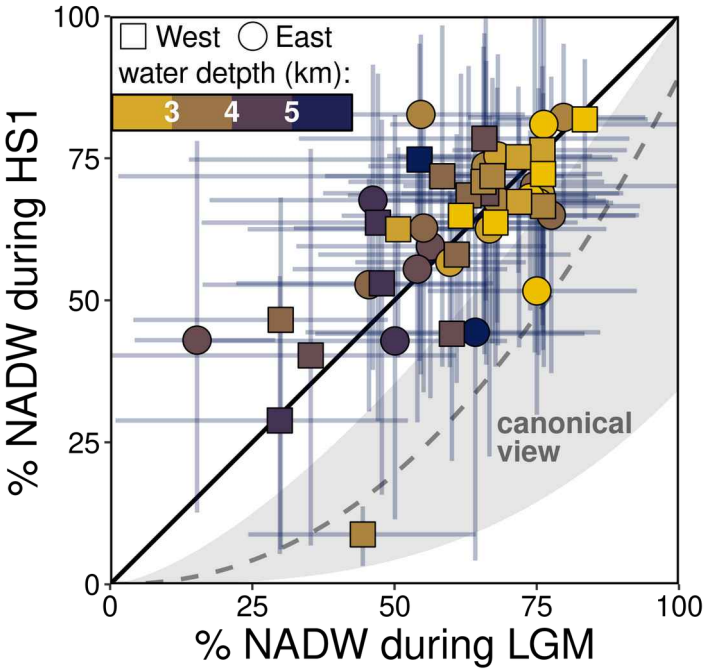


301

***Fig. 4:*** *Mixing model ensemble results for NADW prevalence in the Atlantic during LGM and HS1. Results are averaged for each model box from > 1000 model runs for each time period. Error bars indicate 95 % ranges. Black line shows 1:1 ratio. Symbol shapes distinguish West- from East Atlantic and fill colours indicate water depth. Grey area qualitatively indicates the field in which data are expected to lie if there had been a strong reduction of NADW prevalence during HS1.*

302

# Methods

## New carbon and oxygen stable isotope data

We created a new record of stable oxygen and carbon isotope signatures from benthic foraminifera spanning the last 22 ka at Site IODP U1302 from the deep Labrador Sea (50.2 °N, 45.6 °W, 3556 m water depth; Channell et al., 2012), which is a key region for the assessment of the properties and mixing of l-NADW.

To reconstruct the archived stable oxygen and carbon isotope signatures we selected 3-8 fossil specimens of the epifaunal benthic foraminifer species *Cibicidoides wuellerstorfi or* the shallow infaunal species and *Hoeglundia elegans* and *Uvigerina peregrina* from the >106 µm grain-size fraction. The alternating use of these three species was necessary as none of the species were consistently present throughout the studied sediment interval.

Prior to measurement, the selected foraminifer tests were carefully crushed, ultrasonicated in methanol to physically remove contaminations (e.g., clays and nannofossils) and subsequently dried at 50°C. The stable isotope measurements were carried out on a MicroMass Isoprime mass-spectrometer at the Geotop-UQAM, Canada. The precision of the measurements is ±0.05 ‰ for $\delta^{13}C$ and $\delta^{18}O$ (one standard deviation uncertainty in the analysis of standards). The results were calibrated using the international standard NBS-19 ($\delta^{18}O$ = 2.20 ‰ and $\delta^{13}C$ = 1.95 ‰; Coplen, 1988), and two in-house standards. Isotopic values are reported in standard delta notation (δ) relative to the Vienna Pee Dee Belemnite (VPDB). The non-*Cibicides* isotope data from this site were corrected for species-specific offsets as described below.

Additionally, a number of LH, HS1 and LGM *Cibicides* $\delta^{18}O_b$ and $\delta^{13}C_b$ values are derived from new records that were produced during the ACCLIMATE project and consistently dated as described in Waelbroeck et al. (2019) (age models can be downloaded from https://www.seanoe.org/data/00484/59554/). Epifaunal benthic foraminifers of the *Cibicides* genus were hand picked in the > 150 µm size fraction. *C. wuellerstorfi* samples were picked when possible and treated like described above.

*Cibicides* oxygen and carbon isotope ratios for these samples were measured at LSCE on a MicroMass Isoprime100 mass-spectrometer on samples of 1 to 5 specimens using the NBS-19 standard relative to VPDB. The mean external reproducibility of carbonate standards was 0.05 ‰ for $\delta^{18}O$ and 0.03 ‰ (one standard deviation) for $\delta^{13}C$; measured NBS-18 $\delta^{18}O$ was -23.27 ± 0.10 ‰ VPDB and $\delta^{13}C$ was -5.01 ± 0.03 ‰VPDB.

## Glacial Atlantic water mass proxy data base

Proxy data for Atlantic deep water stable isotope signatures ($\delta^{13}C_b$ & $\delta^{18}O_b$), [$CO_3^{2-}$] inferred from B/Ca ratios, and radiocarbon ventilation age ($^{14}C_{b\text{-}atm}$) - all measured on benthic foraminifera calcite - as well as radiogenic Nd isotope signatures (εNd) extracted from authigenic sediment phases via dissolution of foraminifera or acid-reductive bulk sediment leaching, were compiled from this study and several original publications and compilations (Blaser et al., 2020; Du et al., 2020; Duplessy et al., 2001; Howe et al., 2016; Jonkers et al., 2020; Oppo et al., 2018; Repschläger et al., 2021; Skinner et al., 2021; Yu et al., 2020; Zhao et al., 2018). For C and O isotopes and B/Ca, only

foraminifera from the *Cibicides* genus were used for the Atlantic-wide compilation, preferably *C. wuellerstorfi*. Nd isotope data from five sites from the eastern subpolar North Atlantic were omitted because it has been suggested that they are compromised by localised non-conservative effects (Blaser et al., 2019; Roberts and Piotrowski, 2015; Vogt-Vincent et al., 2020). The data were averaged for each site for the LGM (23 - 19 ka BP), HS1 (17.5 - 14.6 ka BP), and LH (5 - 0 ka BP) based on the existing age models from the same literature. For completeness we briefly describe each proxy in Supplementary Text 1.

## Species-specific corrections for oxygen and carbon stable isotope data

For the Atlantic-wide source water estimates only *Cibicides*-derived $\delta^{13}C_b$ & $\delta^{18}O_b$ data were used, which are precipitated in equilibrium with seawater. However, records based on *Cibicides* are not available for all regions and depths relevant for the discussion and definition of glacial NADW components in the high northern latitudes (Fig. 1). Therefore, we included stable oxygen and carbon isotope records from other species in addition to those from *Cibicides* data, and applied constant interspecies corrections in order to account for species-specific fractionation in oxygen and carbon isotopes. We assumed that isotopes in the shells of *C. wuellerstorfi* are precipitated without biological fractionation and followed Shackleton et al. (1984) by applying a constant fractionation factor of -0.64 ‰ for $\delta^{18}O_b$ and +0.9 ‰ for the $\delta^{13}C_b$ values of *U. peregrina* (Site U1302). *H. elegans* (Site U1302, but not used for this study) was corrected by applying a constant fractionation factor of +0.24 ‰ and +1.5 ‰ for $\delta^{18}O_b$ and $\delta^{13}C_b$, respectively (McCorkle et al., 1997). *Cassidulina neoteretis* data from Site HH15-1252PC (El bani Altuna et al., 2021) and *Cassidulina teretis* data from Site MD95-2010 (Dokken and Jansen, 1999) were assumed to be equally offset from equilibrium and corrected by -0.64 ‰ for $\delta^{18}O_b$ values (Dokken and Jansen, 1999) and +1.5 ‰ for $\delta^{13}C_b$. The correction for $\delta^{13}C_b$ was obtained by alignment of data between data from site MD95-2010 and *Cibicides*-derived data from site PS2644 between 11 to 12.5 ka. This last correction certainly bears the largest potential for bias, but it is noteworthy that the overall interpretations related to Fig. 1 and the definition of the different components of NADW does not exclusively rely on data from non-*Cibicides*, species, and would not change if only data from *Cibicides* records were considered.

## Correction of $\delta^{18}O$ data

All $\delta^{18}O_b$ values reported are corrected for global ice volume ($\delta^{18}O_{b,ivc}$) by converting contemporary sea level relative to modern to a related change in global marine $\delta^{18}O$. To this end we used the sea level curve from Grant et al. (2012) and assumed a sensitivity of 1.05 ‰ / 110 m sea level change (i.e. during the LGM), in order to allow comparison across time periods (Extended Data Fig. 4). Note, however, that the accuracy and consistency of this correction depends on the quality of the age models. This is particularly true for time intervals during which global sea level underwent drastic changes, such as the MIS2 – MIS1 transition. In the time intervals around the LGM and HS1, inaccuracies in the age models of 0.5 and 1.0 ka can lead to biases in the $\delta^{18}O_{b,ivc}$ signals of up to 0.05 and 0.1 ‰, respectively (Extended Data Fig. 4), which we interpret as minor compared to measurement and offset correction uncertainties .

It has been shown that analyses of oxygen isotope data from foraminifera may suffer from systematic biases due to gas mixing in the mass spectrometer source or other non-ideal instrument performance (Ostermann and Curry, 2000; Repschläger et al., 2021). Assuming that such biases can

be considered to be constant along a given $\delta^{18}O_b$ record, we corrected the measured signals by a constant site-specific offset that minimises the difference between Late Holocene (here younger than 4 ka BP if available, or else < 6 ka or < 8 ka) data and the equilibrium *Cibicides* $\delta^{18}O_b$ values computed from local seawater $\delta^{18}O$ and temperature according to equation 9 from Marchitto et al. (2014). Local seawater $\delta^{18}O$ in turn was inferred from local seawater salinity and basin- and depth-specific linear regressions of sea water $\delta^{18}O$ vs. salinity (Supplementary Table 5 & Extended Data Fig. 5). The regressions were generated from the GISS seawater $\delta^{18}O$ data set (Bigg and Rohling, 2000; Schmidt, 1999; Schmidt et al., 2018). Local seawater temperature and salinity were interpolated from WOA13 gridded global data set.

The offsets between late Holocene foraminifera $\delta^{18}O_b$ and equilibrium *Cibicides* $\delta^{18}O_b$ average to a slightly positive value of 0.19 ± 0.56 ‰ (2 standard deviations, n = 104). By adding these constant site-specific offsets, glacial $\delta^{18}O_{b,ivc}$ values are therefore in average shifted towards slightly higher values and low outliers are reduced (Extended Data Fig. 6). The data thus appear more consistent. In particular, the data spread in water depths between 2 and 4 km is reduced. For example, uncorrected LGM $\delta^{18}O_{b,ivc}$ data across the Atlantic below 2 km water depth average to 3.27 ± 0.54 ‰, and offset-corrected data ($\delta^{18}O_{b,ivoc}$) to 3.60 ± 0.49 ‰. Importantly, we tested the effect of this correction on the mixing calculations (not shown). The reduced data spread tends to decrease the contribution of low-$\delta^{18}O_{b,ivoc}$ (mode 2) source waters in the mixing results.

## ***simmr*** **multi proxy mixing analyses**

We estimated relative contributions of different source waters in the Atlantic from the multi-proxy data set with the *simmr* package for R software (Parnell et al., 2013; Parnell and Inger, 2016). *simmr* is a Bayesian stable isotope mixing model using Gibbs sampling and Marcov chain Monte Carlo simulation and was originally developed for isotopic mixing calculations in ecological feeding studies, but can be directly applied to other mixing scenarios as well. Basically, starting from an a priori source probability distribution, *simmr* repeatedly samples the proxy space semi-randomly and tries to find mixing proportions of defined sources that suit the observation(s). Proxy uncertainties of sources are included, but not those of individual observations. Prior distributions can be used in the form of suggested source water contribution probability distributions to improve the calculations with additional knowledge of the mixing system. Fixed proxy concentrations can be included and are here used in the form of DIC for $\delta^{13}C$ and $^{14}C$ ventilation age and Nd concentrations for εNd in the different source waters. The method can cope with an arbitrary number of sources and proxies, but the larger the number of sources compared to proxies the more uncertain the results will be.

*simmr* results are given as probability distributions from which we calculated summary statistics (see Supplementary Figs. 5 – 16 for visualisations of example model outputs). The choice of sources is critical (see below) and systematically affects the resulting mixing proportions. In our approach, we subdivide the deep Atlantic into 5 depth layers (0.5 km steps from 2 to 4 km water depth, and one box from 4 km to the deepest site at 5.01 km) and 8 ocean basins (eastern subpolar North Atlantic (SPE), western subpolar North Atlantic (SPW), NE, NW, equatorial East (EE), Equatorial West (EW), SE, and SW Atlantic, see Extended Data Fig. 1), resulting in 31 boxes containing observations during the LGM and HS1. We solve the *simmr* model for each box completely independently, so that the results between boxes are only linked via the intrinsic connection in the proxy data.

The model ensemble contains 3000 differently parametrised *simmr* simulations for each box, picked semi-randomly from the three time slices and different combinations of modifications in order to incorporate variations of the model systematics, non-conservative proxy behaviour, and exclusions of individual proxies or source waters (see Extended Data Table 1). We regard the final model ensemble as representative of a large range of potential past source water distributions that generally incorporates the limited knowledge about past non-conservative effects, sampling biases, source water properties, and transient changes within each time period. See Extended Data Fig. 3 for a synthesis of different mixing model results, Supplementary Fig. 4 for model quality assessment via Taylor Diagrams, and Supplementary Figs. 9 & 10 for comparisons of different model results across time periods.

## Mixing model validity

The principal validity of the multi proxy mixing model was assessed with a direct comparison of its performance in estimating NADW abundance from oceanographic parameters with estimates from an optimised multi parameter analysis (OMPA, see Extended Data Fig. 7 and de Carvalho Ferreira and Kerr, 2017). The direct comparison shows very good agreement of both methods even though we did not compensate for nutrient generation through remineralisation of organic matter, which is commonly performed in OMPA analysis.

We performed the same analysis using proxy data in seawater (not shown) in order to estimate the predictive capacity of the individual proxies for NADW abundance in the modern setting (Extended Data Fig. 8). This analysis shows that oxygen isotope signatures are not useful to disentangle NADW from AABW today, and this proxy was therefore excluded from the multi proxy reconstructions for the Late Holocene.

Finally, the most comprehensive assessment of the validity of our multi proxy mixing model approach comes from the comparison between Late Holocene estimates of NADW abundance (77 ± 20 %) compared to that from OMPA (82 %; Fig. 3). Within the broad model ensemble spread the two systematically different calculations agree well. The median of our reconstructions is biased to lower values by 5 %, which is insignificant compared to the overall uncertainty, but which could indicate that the LGM and HS1 estimates of NADW abundance are also slightly biased to too low values. Importantly, also the differentiation between upper and lower NADW (Fig. 3) is achieved rather well, yielding further confidence in the general approach.

## Cost function

In order to evaluate model fit (for example in Supplementary Figs. 9 & 10) we chose a cost function that resembles the commonly used mean absolute error (MAE), but expanded it to include an evaluation across all proxies, the average mean absolute error ($\overline{\mathrm{MAE}}$):

$$\overline{MAE} = 1/N_p \sum_p \sum_j \frac{|x_{p,j} - x_{p,model}|}{\Delta_p}$$

Here, p denotes different proxies, $N_p$ the number of proxies in the respective mixing model run, j the different sedimentary observations of proxy p in the respective mixing model box, $x_{p,model}$ the mean proxy value of the respective model box calculated from the mixing model-derived source water fractions, and $\Delta_p$ the absolute value range of the respective proxy in the glacial source water signatures (see Fig. 2 and Supplementary Table 3). See Supplementary Fig. 4 for a more detailed

view of goodness of fit with the help of Taylor Diagrams and to see how the best 10% of ensemble results of our cost function relate to other measures of goodness of fit.

## Source waters

The choice of potential source waters and their characteristics such as proxy signatures and concentrations are decisive for the outcome of the proxy mixing model. Here, we defined six source waters for the LGM and HS1 Atlantic, in addition to three source waters for the Late Holocene and modern (Fig. 2 and Supplementary Tables 3 and 4). Out of the six glacial source waters, three have already been described in considerable detail in the literature (AABW, PDW, u-NADW), although not all relevant proxy signatures have necessarily been ascribed (see main text and e.g. Du et al., 2020; Howe et al., 2016; Lund et al., 2015; Oppo et al., 2018, 2015; Oppo and Lehman, 1993; Skinner et al., 2021; Toucanne et al., 2021; Yu et al., 2020; Zhao et al., 2019). u-NADW-2 has essentially been described in the same literature, although it was not generally considered an actual source water, or was taken as glacial Antarctic Intermediate Water. Its characteristic deviations in proxy signatures from u-NADW-1 have been explained by some combination of replacement by SSW, increased carbon remineralisation, or meteoric water admixture (Lund et al., 2015; Oppo et al., 2015; Thornalley et al., 2011, 2010).

We estimated the remaining source water properties from actual glacial proxy data distributions in regions near the source water origins. However, it is important to note that this method of property estimation is inherently associated with some degree of subjectivity and that in cases where high quality proxy data from the actual source regions and depths are missing, the true past source water proxy signatures could have been different, and in particular more extreme (i.e. farther from the observations) than the values ascribed. This latter fact introduces uncertainty in particular for the radiocarbon ventilation ages and carbonate ion concentrations of northern sourced deep waters, and for the Nd isotope signatures of AMW because its signature may change within the subpolar North Atlantic (Blaser et al., 2020; Lacan and Jeandel, 2005; Roberts and Piotrowski, 2015). However, these uncertainties are reflected in our estimations of standard errors for the source water proxy signatures (see Fig. 2), which are fully accounted for in the *simmr* model.

Apart from the actual source water proxy signatures the concentrations with which the proxies are transported in the respective source waters affect the mixing results. This is particularly relevant for Nd, whose concentration in intermediate to deep waters today varies roughly by a factor of 2 and can be affected by climatically induced changes in continental weathering. To a much lesser degree it also affects DIC (the relevant concentration for $\delta^{13}C_b$ and radiocarbon), which varies by roughly 10 % in today's open oceans. Additionally, none of these concentrations can currently be directly reconstructed and they are thus essentially unknown for the considered source waters, although several studies have estimated past DIC (e.g. (Boyle, 1988; Oppo et al., 2018; Yu et al., 2020). We therefore initially assume modern-like concentrations for all source waters. For DIC we adopted suggested concentrations for PDW, AABW, and NAIW from (Yu et al., 2020). We furthermore assume the uncertainty in Nd concentration to be so much larger than that for DIC that the latter is practically unimportant for the model outcomes. And finally, we suggest that the concentration of Nd in AMW is the least constrained, since the production of this source water and the weathering regime in its source region were presumably most different from today (Pöppelmeier et al., 2022). Hence, we incorporated a series of modifications, varying the Nd concentration of AMW or alternatively equalising the Nd concentration for all source waters (see Extended Data Table 1).

The following nomenclature for the volumetric contributions of northern source water is used in this study:

NADW = u-NADW + l-NADW = NADW-1 + NADW-2

u-NADW = u-NADW-1 + u-NADW-2

l-NADW = l-NADW-1 + l-NADW-2

NADW-1 = u-NADW-1 + l-NADW-1

NADW-2 = u-NADW-2 + l-NADW-2

Furthermore, l-NADW is assumed to be a mixture of AMW and u-NADW (see Fig. 1). The mixture is determined by the fractional entrainment factor $\phi$:

$$\text{l-NADW} = (1 - \phi) * \text{AMW} + \phi * \text{u-NADW}$$

As a necessary simplification, the entrainment of waters less dense than u-NADW is neglected and entrainment is assumed to be $\phi = 0.55 \pm 0.05$, roughly following (Dickson and Brown, 1994).

## References


Bigg, G.R., Rohling, E.J., 2000. An oxygen isotope data set for marine waters. Journal of Geophysical Research: Oceans 105, 8527–8535. https://doi.org/10.1029/2000JC900005

Blaser, P., Gutjahr, M., Pöppelmeier, F., Frank, M., Kaboth-Bahr, S., Lippold, J., 2020. Labrador Sea bottom water provenance and REE exchange during the past 35,000 years. Earth and Planetary Science Letters 542, 116299. https://doi.org/10.1016/j.epsl.2020.116299

Blaser, P., Pöppelmeier, F., Schulz, H., Gutjahr, M., Frank, M., Lippold, J., Heinrich, H., Link, J.M., Hoffmann, J., Szidat, S., Frank, N., 2019. The resilience and sensitivity of Northeast Atlantic deep water εNd to overprinting by detrital fluxes over the past 30,000 years. Geochimica et Cosmochimica Acta 245, 79–97. https://doi.org/10.1016/j.gca.2018.10.018

Bower, A., Lozier, S., Biastoch, A., Drouin, K., Foukal, N., Furey, H., Lankhorst, M., Rühs, S., Zou, S., 2019. Lagrangian Views of the Pathways of the Atlantic Meridional Overturning Circulation. Journal of Geophysical Research: Oceans 124, 5313–5335. https://doi.org/10.1029/2019JC015014

Boyle, E.A., 1988. Cadmium: Chemical tracer of deepwater paleoceanography. Paleoceanography 3, 471–489. https://doi.org/10.1029/PA003i004p00471

Bradtmiller, L.I., McManus, J.F., Robinson, L.F., 2014. 231Pa/230Th evidence for a weakened but persistent Atlantic meridional overturning circulation during Heinrich Stadial 1. Nature Communications 5, 5817. https://doi.org/10.1038/ncomms6817

Channell, J.E.T., Hodell, D.A., Romero, O., Hillaire-Marcel, C., de Vernal, A., Stoner, J.S., Mazaud, A., Röhl, U., 2012. A 750-kyr detrital-layer stratigraphy for the North Atlantic (IODP Sites U1302–U1303, Orphan Knoll, Labrador Sea). Earth and Planetary Science Letters 317–318, 218–230. https://doi.org/10.1016/j.epsl.2011.11.029

Coplen, T.B., 1988. Normalization of oxygen and hydrogen isotope data. Chemical Geology: Isotope Geoscience section 72, 293–297. https://doi.org/10.1016/0168-9622(88)90042-5

Curry, W.B., Duplessy, J.C., Labeyrie, L.D., Shackleton, N.J., 1988. Changes in the distribution of δ13C of deep water ΣCO2 between the Last Glaciation and the Holocene. Paleoceanography 3, 317–341. https://doi.org/10.1029/PA003i003p00317

de Carvalho Ferreira, M.L., Kerr, R., 2017. Source water distribution and quantification of North Atlantic Deep Water and Antarctic Bottom Water in the Atlantic Ocean. Progress in Oceanography 153, 66–83. https://doi.org/10.1016/j.pocean.2017.04.003

Dickson, R.R., Brown, J., 1994. The production of North Atlantic Deep Water: Sources, rates, and pathways. Journal of Geophysical Research: Oceans 99, 12319–12341. https://doi.org/10.1029/94JC00530

Dokken, T.M., Jansen, E., 1999. Rapid changes in the mechanism of ocean convection during the last glacial period. Nature 401, 458–461. https://doi.org/10.1038/46753

Du, J., Haley, B.A., Mix, A.C., 2020. Evolution of the Global Overturning Circulation since the Last Glacial Maximum based on marine authigenic neodymium isotopes. Quaternary Science Reviews 241, 106396. https://doi.org/10.1016/j.quascirev.2020.106396

Duplessy, J.-C., Labeyrie, L., Waelbroeck, C., 2001. Constraints on the ocean oxygen isotopic enrichment between the Last Glacial Maximum and the Holocene: Paleoceanographic implications. Quaternary Science Reviews, EPILOG 21, 315–330. https://doi.org/10.1016/S0277-3791(01)00107-X

El bani Altuna, N., Ezat, M.M., Greaves, M., Rasmussen, T.L., 2021. Millennial-Scale Changes in Bottom Water Temperature and Water Mass Exchange Through the Fram Strait 79°N, 63-13 ka. Paleoceanography and Paleoclimatology 36, e2020PA004061. https://doi.org/10.1029/2020PA004061

Evans, H.K., Hall, I.R., 2008. Deepwater circulation on Blake Outer Ridge (western North Atlantic) during the Holocene, Younger Dryas, and Last Glacial Maximum. Geochemistry, Geophysics, Geosystems 9. https://doi.org/10.1029/2007GC001771

Ezat, M.M., Rasmussen, T.L., Hain, M.P., Greaves, M., Rae, J.W.B., Zamelczyk, K., Marchitto, T.M., Szidat, S., Skinner, L.C., 2021. Deep Ocean Storage of Heat and CO2 in the Fram Strait, Arctic Ocean During the Last Glacial Period. Paleoceanography and Paleoclimatology 36, e2021PA004216. https://doi.org/10.1029/2021PA004216

Grant, K.M., Rohling, E.J., Bar-Matthews, M., Ayalon, A., Medina-Elizalde, M., Ramsey, C.B., Satow, C., Roberts, A.P., 2012. Rapid coupling between ice volume and polar temperature over the past 150,000 years. Nature 491, 744–747. https://doi.org/10.1038/nature11593

Gutjahr, M., Hoogakker, B.A.A., Frank, M., McCave, I.N., 2010. Changes in North Atlantic Deep Water strength and bottom water masses during Marine Isotope Stage 3 (45–35kaBP). Quaternary Science Reviews 29, 2451–2461. https://doi.org/10.1016/j.quascirev.2010.02.024

Hines, S.K.V., Bolge, L., Goldstein, S.L., Charles, C.D., Hall, I.R., Hemming, S.R., 2021. Little Change in Ice Age Water Mass Structure From Cape Basin Benthic Neodymium and Carbon Isotopes. Paleoceanography and Paleoclimatology 36, e2021PA004281. https://doi.org/10.1029/2021PA004281

Howe, J.N.W., Piotrowski, A.M., Noble, T.L., Mulitza, S., Chiessi, C.M., Bayon, G., 2016. North Atlantic Deep Water Production during the Last Glacial Maximum. Nature Communications 7, 11765. https://doi.org/10.1038/ncomms11765

Johnson, G.C., 2008. Quantifying Antarctic Bottom Water and North Atlantic Deep Water volumes. Journal of Geophysical Research: Oceans 113. https://doi.org/10.1029/2007JC004477

Jonkers, L., Cartapanis, O., Langner, M., McKay, N., Mulitza, S., Strack, A., Kucera, M., 2020. Integrating palaeoclimate time series with rich metadata for uncertainty modelling: strategy and documentation of the PalMod 130k marine palaeoclimate data synthesis. Earth System Science Data 12, 1053–1081. https://doi.org/10.5194/essd-12-1053-2020

Keigwin, L.D., Swift, S.A., 2017. Carbon isotope evidence for a northern source of deep water in the glacial western North Atlantic. Proceedings of the National Academy of Sciences 114, 2831–2835. https://doi.org/10.1073/pnas.1614693114

Khatiwala, S., Schmittner, A., Muglia, J., 2019. Air-sea disequilibrium enhances ocean carbon storage during glacial periods. Science Advances 5, eaaw4981. https://doi.org/10.1126/sciadv.aaw4981

Labeyrie, L., Waelbroeck, C., Cortijo, E., Michel, E., Duplessy, J.-C., 2005. Changes in deep water hydrology during the Last Deglaciation. Comptes Rendus Geoscience 337, 919–927. https://doi.org/10.1016/j.crte.2005.05.010

Lacan, F., Jeandel, C., 2005. Acquisition of the neodymium isotopic composition of the North Atlantic Deep Water. Geochemistry, Geophysics, Geosystems 6. https://doi.org/10.1029/2005GC000956

Lippold, J., Luo, Y., Francois, R., Allen, S.E., Gherardi, J., Pichat, S., Hickey, B., Schulz, H., 2012. Strength and geometry of the glacial Atlantic Meridional Overturning Circulation. Nature Geoscience 5, 813–816. https://doi.org/10.1038/ngeo1608

Lund, D.C., Tessin, A.C., Hoffman, J.L., Schmittner, A., 2015. Southwest Atlantic water mass evolution during the last deglaciation. Paleoceanography 30, 477–494. https://doi.org/10.1002/2014PA002657

Lynch-Stieglitz, J., 2017. The Atlantic Meridional Overturning Circulation and Abrupt Climate Change. Annual Review of Marine Science 9, 83–104. https://doi.org/10.1146/annurev-marine-010816-060415

Mackensen, A., 2012. Strong thermodynamic imprint on Recent bottom-water and epibenthic δ13C in the Weddell Sea revealed: Implications for glacial Southern Ocean ventilation. Earth and Planetary Science Letters 317–318, 20–26. https://doi.org/10.1016/j.epsl.2011.11.030

Marchitto, T.M., Curry, W.B., Lynch-Stieglitz, J., Bryan, S.P., Cobb, K.M., Lund, D.C., 2014. Improved oxygen isotope temperature calibrations for cosmopolitan benthic foraminifera. Geochimica et Cosmochimica Acta 130, 1–11. https://doi.org/10.1016/j.gca.2013.12.034

Marcott, S.A., Clark, P.U., Padman, L., Klinkhammer, G.P., Springer, S.R., Liu, Z., Otto-Bliesner, B.L., Carlson, A.E., Ungerer, A., Padman, J., He, F., Cheng, J., Schmittner, A., 2011. Ice-shelf collapse from subsurface warming as a trigger for Heinrich events. PNAS 108, 13415–13419. https://doi.org/10.1073/pnas.1104772108

Marshall, J., Speer, K., 2012. Closure of the meridional overturning circulation through Southern Ocean upwelling. Nature Geosci 5, 171–180. https://doi.org/10.1038/ngeo1391

McCorkle, D.C., Corliss, B.H., Farnham, C.A., 1997. Vertical distributions and stable isotopic compositions of live (stained) benthic foraminifera from the North Carolina and California continental margins. Deep Sea Research Part I: Oceanographic Research Papers 44, 983–1024. https://doi.org/10.1016/S0967-0637(97)00004-6

McManus, J.F., Francois, R., Gherardi, J.-M., Keigwin, L.D., Brown-Leger, S., 2004. Collapse and rapid resumption of Atlantic meridional circulation linked to deglacial climate changes. Nature 428, 834–837. https://doi.org/10.1038/nature02494

Meland, M.Y., Dokken, T.M., Jansen, E., Hevrøy, K., 2008. Water mass properties and exchange between the Nordic seas and the northern North Atlantic during the period 23-6 ka: Benthic oxygen isotopic evidence. Paleoceanography 23. https://doi.org/10.1029/2007PA001416

Millo, C., Sarnthein, M., Voelker, A., Erlenkeuser, H., 2006. Variability of the Denmark Strait Overflow during the Last Glacial Maximum. Boreas 35, 50–60. https://doi.org/10.1080/03009480500359244

Ng, H.C., Robinson, L.F., McManus, J.F., Mohamed, K.J., Jacobel, A.W., Ivanovic, R.F., Gregoire, L.J., Chen, T., 2018. Coherent deglacial changes in western Atlantic Ocean circulation. Nature Communications 9, 2947. https://doi.org/10.1038/s41467-018-05312-3

Oppo, D.W., Curry, W.B., McManus, J.F., 2015. What do benthic δ13C and δ18O data tell us about Atlantic circulation during Heinrich Stadial 1? Paleoceanography 30, 353–368. https://doi.org/10.1002/2014PA002667

Oppo, D.W., Gebbie, G., Huang, K.-F., Curry, W.B., Marchitto, T.M., Pietro, K.R., 2018. Data Constraints on Glacial Atlantic Water Mass Geometry and Properties. Paleoceanography and Paleoclimatology 33, 1013–1034. https://doi.org/10.1029/2018PA003408

Oppo, D.W., Lehman, S.J., 1993. Mid-Depth Circulation of the Subpolar North Atlantic During the Last Glacial Maximum. Science 259, 1148–1152. https://doi.org/10.1126/science.259.5098.1148

Ostermann, D.R., Curry, W.B., 2000. Calibration of stable isotopic data: An enriched δ18O standard used for source gas mixing detection and correction. Paleoceanography 15, 353–360. https://doi.org/10.1029/1999PA000411

Parnell, A.C., Inger, R., 2016. Simmr: a stable isotope mixing model.

Parnell, A.C., Phillips, D.L., Bearhop, S., Semmens, B.X., Ward, E.J., Moore, J.W., Jackson, A.L., Grey, J., Kelly, D.J., Inger, R., 2013. Bayesian stable isotope mixing models. Environmetrics 24, 387–399. https://doi.org/10.1002/env.2221

Petit, T., Lozier, M.S., Josey, S.A., Cunningham, S.A., 2020. Atlantic Deep Water Formation Occurs Primarily in the Iceland Basin and Irminger Sea by Local Buoyancy Forcing. Geophysical Research Letters 47, e2020GL091028. https://doi.org/10.1029/2020GL091028

Pöppelmeier, F., Blaser, P., Gutjahr, M., Jaccard, S.L., Frank, M., Max, L., Lippold, J., 2020. Northern-sourced water dominated the Atlantic Ocean during the Last Glacial Maximum. Geology 48, 826–829. https://doi.org/10.1130/G47628.1

Pöppelmeier, F., Gutjahr, M., Blaser, P., Keigwin, L.D., Lippold, J., 2018. Origin of Abyssal NW Atlantic Water Masses Since the Last Glacial Maximum. Paleoceanography and Paleoclimatology 33, 530–543. https://doi.org/10.1029/2017PA003290

Pöppelmeier, F., Jeltsch-Thömmes, A., Lippold, J., Joos, F., Stocker, T.F., accepted. Multi-proxy constraints on Atlantic circulation dynamics since the last ice age. Nature Geoscience.

Pöppelmeier, F., Lippold, J., Blaser, P., Gutjahr, M., Frank, M., Stocker, T.F., 2022. Neodymium isotopes as a paleo-water mass tracer: A model-data reassessment. Quaternary Science Reviews 279, 107404. https://doi.org/10.1016/j.quascirev.2022.107404

Price, J.F., O'Neil Baringer, M., 1994. Outflows and deep water production by marginal seas. Progress in Oceanography 33, 161–200. https://doi.org/10.1016/0079-6611(94)90027-2
Repschläger, J., Zhao, N., Rand, D., Lisiecki, L., Muglia, J., Mulitza, S., Schmittner, A., Cartapanis, O., Bauch, H.A., Schiebel, R., Haug, G.H., 2021. Active North Atlantic deepwater formation during Heinrich Stadial 1. Quaternary Science Reviews 270, 107145. https://doi.org/10.1016/j.quascirev.2021.107145
Roberts, N.L., Piotrowski, A.M., 2015. Radiogenic Nd isotope labeling of the northern NE Atlantic during MIS 2. Earth and Planetary Science Letters 423, 125–133. https://doi.org/10.1016/j.epsl.2015.05.011
Schmidt, G.A., 1999. Forward modeling of carbonate proxy data from planktonic foraminifera using oxygen isotope tracers in a global ocean model. Paleoceanography 14, 482–497. https://doi.org/10.1029/1999PA900025
Schmidt, G.A., Bigg, G.R., Rohling, E.J., 2018. Global Seawater Oxygen-18 Database - v1.22 [WWW Document]. URL https://data.giss.nasa.gov/o18data/ (accessed 5.14.21).
Seidenkrantz, M.-S., Kuijpers, A., Aagaard-Sørensen, S., Lindgreen, H., Olsen, J., Pearce, C., 2021. Evidence for influx of Atlantic water masses to the Labrador Sea during the Last Glacial Maximum. Scientific Reports 11, 6788. https://doi.org/10.1038/s41598-021-86224-z
Shackleton, N.J., Backman, J., Zimmerman, H., Kent, D.V., Hall, M.A., Roberts, D.G., Schnitker, D., Baldauf, J.G., Desprairies, A., Homrighausen, R., Huddlestun, P., Keene, J.B., Kaltenback, A.J., Krumsiek, K. a. O., Morton, A.C., Murray, J.W., Westberg-Smith, J., 1984. Oxygen isotope calibration of the onset of ice-rafting and history of glaciation in the North Atlantic region. Nature 307, 620–623. https://doi.org/10.1038/307620a0
Skinner, L.C., Freeman, E., Hodell, D., Waelbroeck, C., Vazquez Riveiros, N., Scrivner, A.E., 2021. Atlantic Ocean Ventilation Changes Across the Last Deglaciation and Their Carbon Cycle Implications. Paleoceanography and Paleoclimatology 36, e2020PA004074. https://doi.org/10.1029/2020PA004074
Stocker, T.F., 2013. Chapter 1 - The Ocean as a Component of the Climate System, in: Siedler, G., Griffies, S.M., Gould, J., Church, J.A. (Eds.), International Geophysics, Ocean Circulation and Climate. Academic Press, pp. 3–30. https://doi.org/10.1016/B978-0-12-391851-2.00001-5
Süfke, F., Pöppelmeier, F., Goepfert, T.J., Regelous, M., Koutsodendris, A., Blaser, P., Gutjahr, M., Lippold, J., 2019. Constraints on the Northwestern Atlantic Deep Water Circulation From 231Pa/230Th During the Last 30,000 Years. Paleoceanography and Paleoclimatology 34, 1945–1958. https://doi.org/10.1029/2019PA003737
Thornalley, D.J.R., Barker, S., Broecker, W.S., Elderfield, H., McCave, I.N., 2011. The Deglacial Evolution of North Atlantic Deep Convection. Science 331, 202–205. https://doi.org/10.1126/science.1196812
Thornalley, D.J.R., Elderfield, H., McCave, I.N., 2010. Intermediate and deep water paleoceanography of the northern North Atlantic over the past 21,000 years. Paleoceanography 25, PA1211. https://doi.org/10.1029/2009PA001833
Toucanne, S., Soulet, G., Vázquez Riveiros, N., Boswell, S.M., Dennielou, B., Waelbroeck, C., Bayon, G., Mojtahid, M., Bosq, M., Sabine, M., Zaragosi, S., Bourillet, J.-F., Mercier, H., 2021. The North Atlantic Glacial Eastern Boundary Current as a Key Driver for Ice-Sheet—AMOC Interactions and Climate Instability. Paleoceanography and Paleoclimatology 36, e2020PA004068. https://doi.org/10.1029/2020PA004068
Vogt-Vincent, N., Lippold, J., Kaboth-Bahr, S., Blaser, P., 2020. Ice-rafted debris as a source of non-conservative behaviour for the εNd palaeotracer: insights from a simple model. Geo-Mar Lett 1–16. https://doi.org/10.1007/s00367-020-00643-x
Waelbroeck, C., Lougheed, B.C., Riveiros, N.V., Missiaen, L., Pedro, J., Dokken, T., Hajdas, I., Wacker, L., Abbott, P., Dumoulin, J.-P., Thil, F., Eynaud, F., Rossignol, L., Fersi, W., Albuquerque, A.L., Arz, H., Austin, W.E.N., Came, R., Carlson, A.E., Collins, J.A., Dennielou, B., Desprat, S., Dickson, A., Elliot, M., Farmer, C., Giraudeau, J., Gottschalk, J.,

Henderiks, J., Hughen, K., Jung, S., Knutz, P., Lebreiro, S., Lund, D.C., Lynch-Stieglitz, J., Malaizé, B., Marchitto, T., Martínez-Méndez, G., Mollenhauer, G., Naughton, F., Nave, S., Nürnberg, D., Oppo, D., Peck, V., Peeters, F.J.C., Penaud, A., Portilho-Ramos, R. da C., Repschläger, J., Roberts, J., Rühlemann, C., Salgueiro, E., Goni, M.F.S., Schönfeld, J., Scussolini, P., Skinner, L.C., Skonieczny, C., Thornalley, D., Toucanne, S., Rooij, D.V., Vidal, L., Voelker, A.H.L., Wary, M., Weldeab, S., Ziegler, M., 2019. Consistently dated Atlantic sediment cores over the last 40 thousand years. Sci Data 6, 1–12. https://doi.org/10.1038/s41597-019-0173-8

Waelbroeck, C., Skinner, L.C., Labeyrie, L., Duplessy, J.-C., Michel, E., Vazquez Riveiros, N., Gherardi, J.-M., Dewilde, F., 2011. The timing of deglacial circulation changes in the Atlantic. Paleoceanography 26. https://doi.org/10.1029/2010PA002007

Williams, T.J., Hillenbrand, C.-D., Piotrowski, A.M., Allen, C.S., Frederichs, T., Smith, J.A., Ehrmann, W., Hodell, D.A., 2019. Paleocirculation and Ventilation History of Southern Ocean Sourced Deep Water Masses During the Last 800,000 Years. Paleoceanography and Paleoclimatology 34, 833–852. https://doi.org/10.1029/2018PA003472

Yu, J., Elderfield, H., Piotrowski, A.M., 2008. Seawater carbonate ion-δ13C systematics and application to glacial–interglacial North Atlantic ocean circulation. Earth and Planetary Science Letters 271, 209–220. https://doi.org/10.1016/j.epsl.2008.04.010

Yu, J., Menviel, L., Jin, Z.D., Anderson, R.F., Jian, Z., Piotrowski, A.M., Ma, X., Rohling, E.J., Zhang, F., Marino, G., McManus, J.F., 2020. Last glacial atmospheric CO 2 decline due to widespread Pacific deep-water expansion. Nature Geoscience 1–6. https://doi.org/10.1038/s41561-020-0610-5

Zhao, N., Marchal, O., Keigwin, L., Amrhein, D., Gebbie, G., 2018. A Synthesis of Deglacial Deep-Sea Radiocarbon Records and Their (In)Consistency With Modern Ocean Ventilation. Paleoceanography and Paleoclimatology 33, 128–151. https://doi.org/10.1002/2017PA003174

Zhao, N., Oppo, D.W., Huang, K.-F., Howe, J.N.W., Blusztajn, J., Keigwin, L.D., 2019. Glacial–interglacial Nd isotope variability of North Atlantic Deep Water modulated by North American ice sheet. Nat Commun 10, 1–10. https://doi.org/10.1038/s41467-019-13707-z

523

524

# Extended data to

# *Prevalent glacial North Atlantic Deep Water despite Arctic freshwater input*

## Content:

***Extended Data* Table 1:** List of *modifications for* the applied *mixing model. Modifications from each row were randomly combined with each other, and 3000 combinations were sampled for the model ensemble.*

| model modification | implementation | values in ensemble | number of occurrences in ensemble |
|---|---|---|---|
| average observations | Average observations for each proxy in each box to one median value in order to remove bias from the number of data per proxy and box. | | 672 |
| offset-correction for all proxies | Correct all observations by their Late Holocene offset from estimated local seawater signatures. | | 375 |
| remove proxy from model | Remove certain proxies from observations and source waters. | each proxy individually, $\delta^{18}O$ and εNd, or all carbon related proxies | 1530 |
| remove source water uncertainty | Set uncertainty of all source water signatures (see Supplementary Table 3) to zero. | | 1288 |
| remove AMW from model | Remove both AMW-1 and AMW-2 completely from potential source waters. | | 593 |
| remove AMW-2 from model | Remove only AMW-2 completely from potential source waters. | | 284 |
| remove mode-2 source waters from model | Remove both u-NADW-2 and AMW-2 completely from potential source waters. | | 325 |
| correct for organic matter remineralisation | Remineralising organic matter exported from the ocean surface adds low $\delta^{13}C$ carbon to the deep DIC pool. We account for this process virtually by adding x ‰ to $\delta^{13}C_b$ observations at depths > 3 km, and 2/3 * x ‰ is added to observations between 2 and 3 km, roughly following the profile of remineralised $\delta^{13}C$ from Oppo et al. (2018) for the LGM. Furthermore, corresponding changes of$[CO_3^{2-}]$ of +43 µmol/kg per ‰ change in $\delta^{13}C_b$ are applied to the same locations, following Yu et al. (2008). | x = {0, 0.1, 0.2, 0.3, 0.4, 0.5} | 1652 |
| correct very low glacial South Atlantic $\delta^{13}C$ observations | In the glacial abyssal South Atlantic, very low $\delta^{13}C_b$ around -1‰ have been argued to not represent ambient seawater. This is corrected for following Yu et al. (2020) by adding x ‰ to the $\delta^{13}C_b$ of glacial AABW (correcting for a habitat effect), or alternatively adding x ‰ to the $\delta^{13}C_b$ and additionally +43 µmol/kg per ‰ of $\delta^{13}C_b$ to its $[CO_3^{2-}]$ (correcting for the Mackensen effect). In both cases, observations of $\delta^{13}C_b$ < -0.75 ‰ are excluded from the mixing calculations. | x = {0, 0.25, 0.5} | 1049 |
| test with different Nd concentrations | The concentration of Nd in past source waters is unknown, and may have been significantly different. This counts in particular for AMW, which was probably the most different from modern analogues and additionally in contact with sediments in the Labrador Sea (Pöppelmeier et al., 2022). The concentration of Nd in AMW is increased by a factor of x, or alternatively Nd concentrations of all source waters are set equal. | x = {1, 1.5, 2, 2.5} | 1606 |
| correct for benthic flux of Nd | Benthic flux of Nd affects water masses in contact with sediment. This is particularly important for abyssal SSW, which is rendered less radiogenic on its northward advance. Hence, εNd of glacial PDW and AABW is decreased by x epsilon units in equatorial, north, and subpolar Atlantic model regions. South Atlantic regions are assumed to be not altered as they represent the actual source waters. | x = {0, 1, 2, 3, 4, 5} | 1725 |
| bias in Northwest and Labrador Sea εNd records | In Holocene sediments, εNd from the deep North American Basin and Labrador Sea is systematically less radiogenic than local bottom water, and it is uncertain to which degree such an effect also occurred during glacials (Pöppelmeier et al., 2019):<br>The εNd of observations in the NW Atlantic and western subpolar North Atlantic from latitude > 22°N and depths >= 3 km and of northern sourced deep waters is increased by x. Alternatively, the εNd of AMW is increased by 3 units, assuming that reconstructions from the Labrador Sea were biased (Blaser et al., 2020). | x = {0, 1, 2, 3, 4, 5} | 1907 |

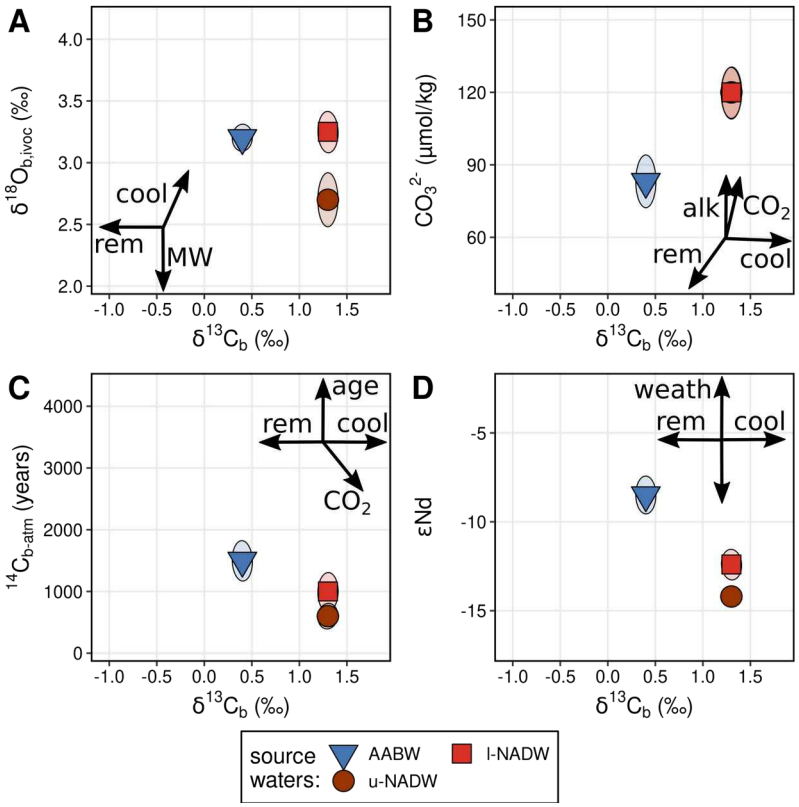


***Extended Data Figure 1:*** *Same as Fig. 2 but for modern and Late Holocene source waters.*

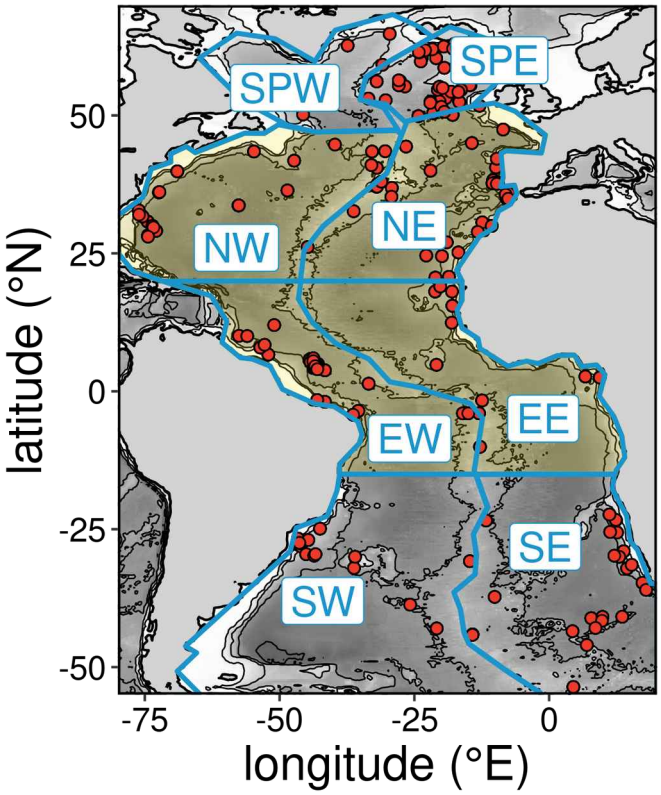


***Extended Data Figure 2:*** *Spatial distribution of proxy data for the LGM and HS1. Red dots indicate positions of sediment cores contributing proxy observations. Different model regions are outlined and labelled (SPW/E = western/eastern subpolar North Atlantic). North Atlantic Deep Water prevalence was assessed for the yellow shaded volume below 2 km modern water depth.*

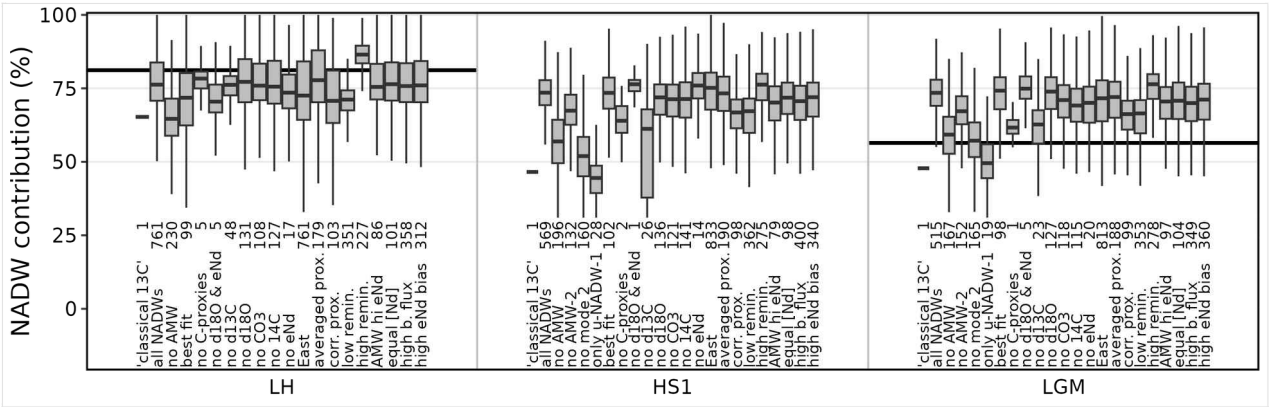


***Extended Data Figure 3:*** *NADW contributions for the deep Atlantic as in Fig. 3 during LH, HS1, and LGM for different ensemble subsets. Numbers indicate the number of runs included in each subset. Background thick horizontal lines in LH and LGM indicate calculations based on optimised multi parameter analysis (de Carvalho Ferreira and Kerr, 2017) and inverse modelling (Oppo et al., 2018), respectively. Small black bars are "classical" scenarios based on exclusively* $\delta^{13}C_b$ *as proxy and AABW and u-NADW-1 as the only source waters.*

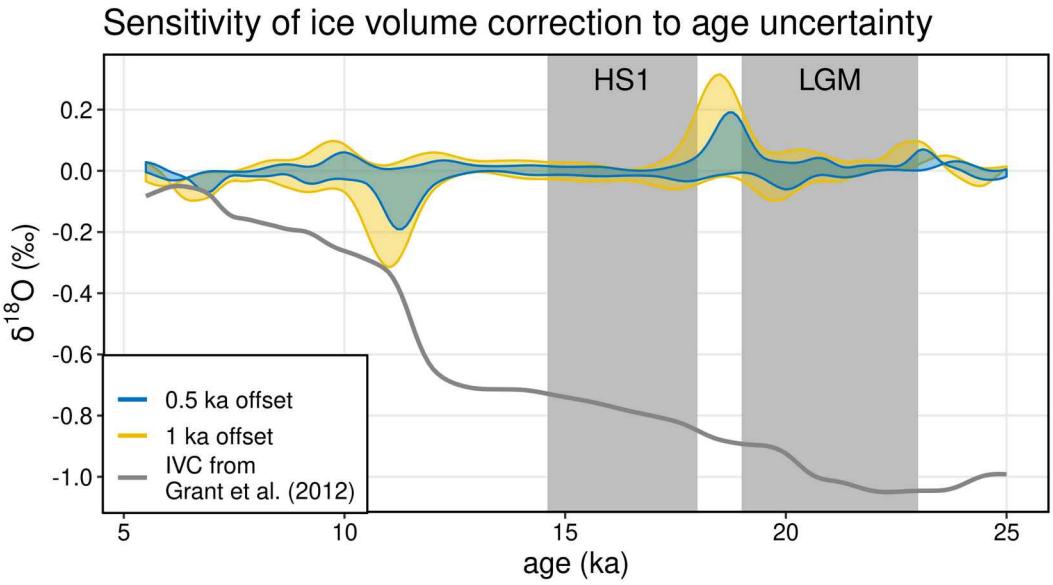


***Extended Data Figure 4:*** *Sensitivity of $\delta^{18}O$ ice volume correction to age uncertainty. Grey curve shows the correction curve applied, based on sea level reconstructions from (Grant et al., 2012), yellow and blue areas are correction biases for age errors of < 1.0 and < 0.5 ka offset, respectively.*

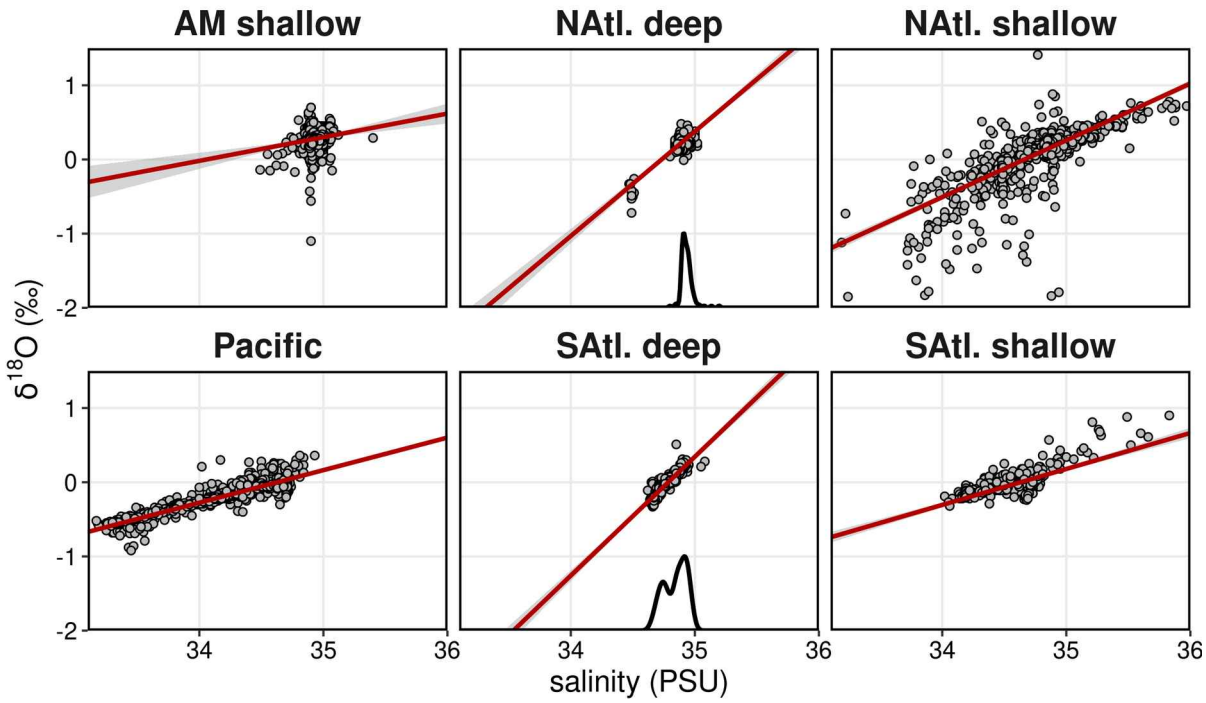


***Extended Data Figure 5:*** *Linear regressions of $\delta^{18}O$ in seawater versus salinity for water depths > 200 m. The panels differentiate different spacial domains. In the central column, black curves indicate probability density distributions of modern salinity at sites contained in the LGM and HS1 data sets for the mixing model (on arbitrary y-axis). See Supplementary Table 5 for regression equations.*

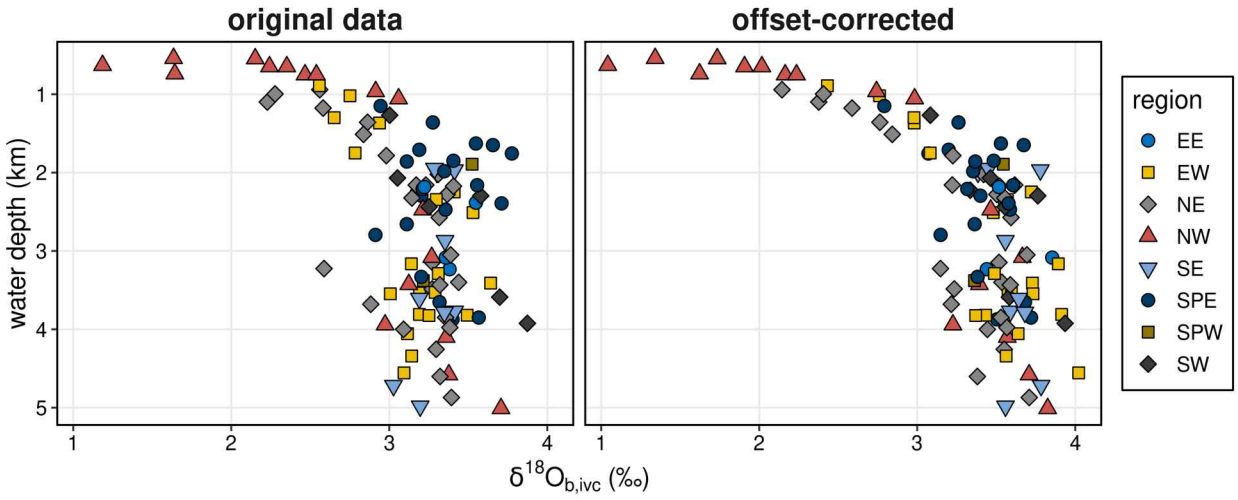


***Extended Data Figure 6:*** *Atlantic LGM benthic $\delta^{18}O_b$ data vs. modern water depth, averaged for each site and ice volume corrected.* ***Left:*** *Original data without further correction.* ***Right:*** *Same data with additional site-specific correction for the offset between Late Holocene data and local seawater. Symbols code the regions where the sediment sites are located.*

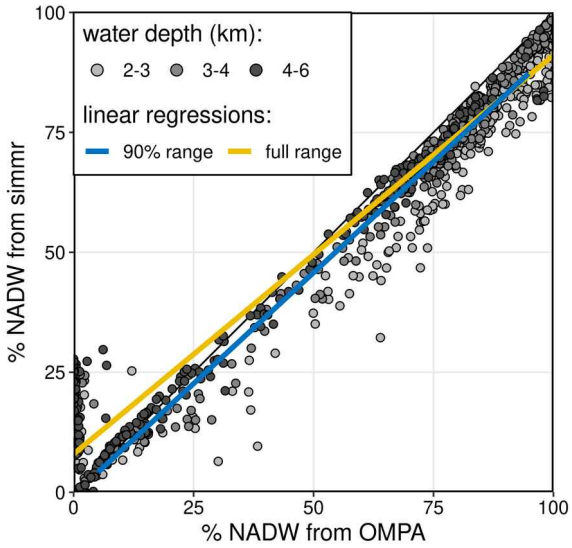


***Extended Data Figure 7:*** *Modern source water identification test with the isotope mixing model used in this study (simmr). In this test, the simmr mixing model using physical and nutrient tracers is compared to published calculations via optimised multi parameter analyses (OMPA) (de Carvalho Ferreira and Kerr, 2017). Blue line shows linear regression excluding the upper- and lowermost 5% of the data. For the simmr calculations no correction for biogenic respiration was performed, explaining part of the discrepancy between both models.*

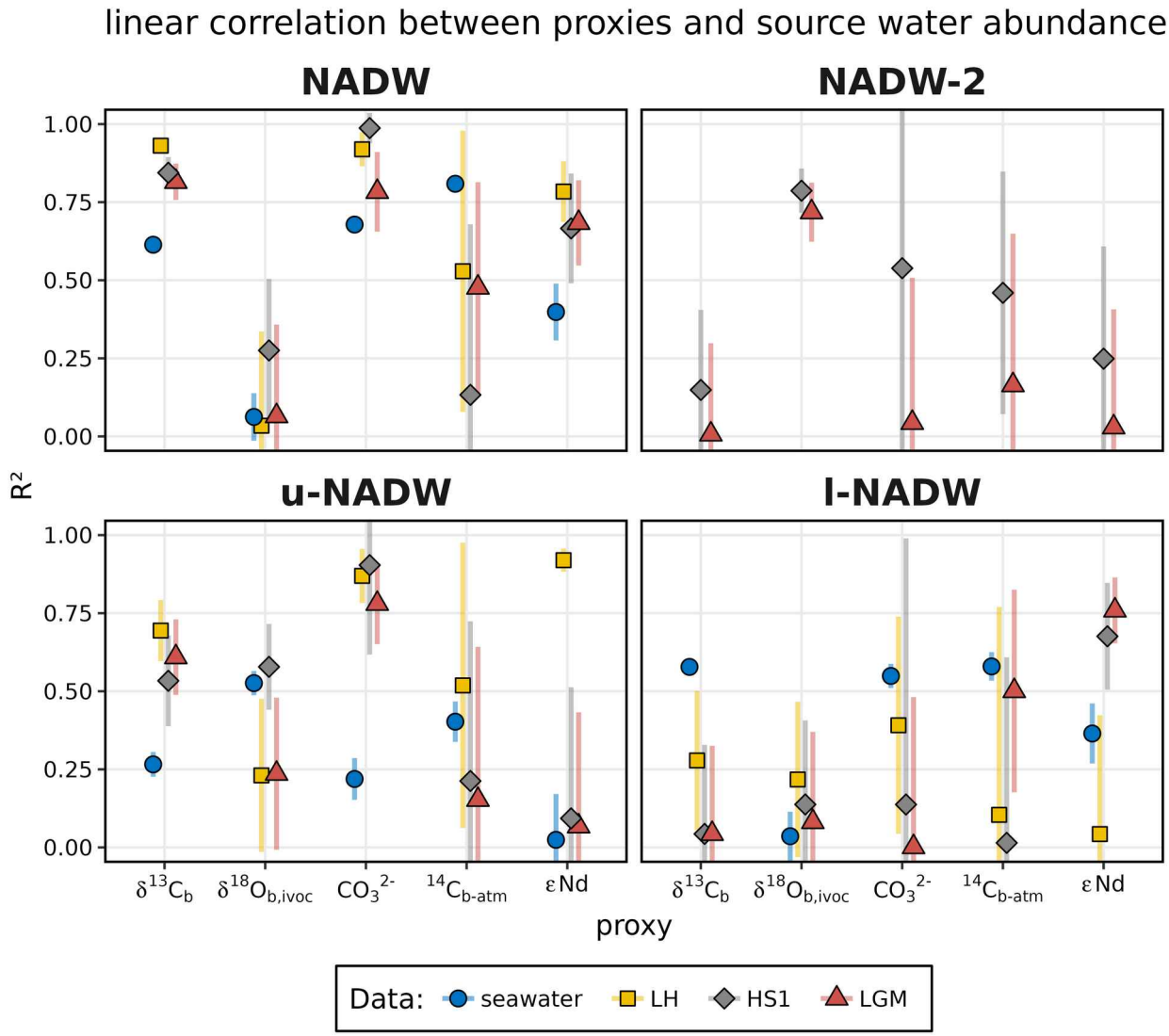


***Extended Data Figure 8:*** *Performance of individual proxies to reconstruct source water contributions. The performance is expressed as linear correlation coefficient R² and its uncertainty (error bars). Different data bases are expressed as colours. For seawater data, actual source water contributions are from (de Carvalho Ferreira and Kerr, 2017). For LH, HS1, and LGM they are estimated from the average from the best 10% of model runs, assessed with the cost function as described in Methods, and proxy data are sedimentary observations. Note that the linear correlation depends on the linearity between the respective proxy and source water type contributions, i.e. on the different source water properties. It is furthermore dependent on the location of proxy observations available for each data set.*

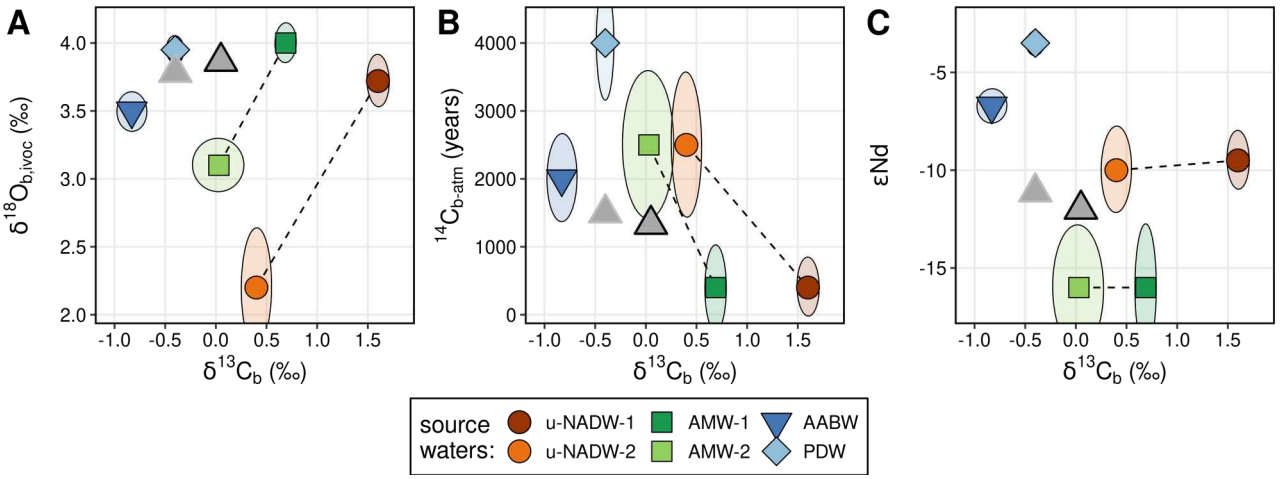


***Extended Data Figure 9:*** *Mixing at abyssal north-west Atlantic Site KNR197-10-17. Same as Figure 2 but without [$CO_3^{2-}$] (because no data exist for the site) and with data for this site shown as grey upwards triangles with black and grey border for LGM and HS1, respectively. Coordinates for KNR197-10-17 are: 48.54°W, 36.405°N, 5010 m water depth* (Keigwin and Swift, 2017; Pöppelmeier et al., 2018).

# Supplement to

# *Prevalent glacial North Atlantic Deep Water despite Arctic freshwater input*

## Contents

# Supplementary Texts

## *Supplementary Text 1:* Proxies used in this study

In the following we give an overview of the five proxies used and discussed in the main text. We also briefly discuss the geochemical processes that are considered in the mixing model (see also Extended Data Table 1).

### Stable carbon isotopes

Stable carbon isotopes have been most widely used for the reconstruction of deep water mass nutrient content and origin. The $\delta^{13}C$ of bottom water dissolved inorganic carbon (DIC) is archived in the carbonate shells of the epibenthic foraminifera genus *Cibicides (Duplessy et al., 1984; Schmittner et al., 2017)*, preserved in marine sediments. The stable carbon isotope signature of seawater is affected by the degree and the temperature of $CO_2$ equilibration between air and surface waters, it is increased by photosynthesis, which discriminates against $^{13}C$, and it is decreased by the remineralisation of organic matter, releasing $^{13}C$ depleted organic compounds to the DIC pool. Since the remineralisation of organic matter also releases the contained nutrients such as phosphate and others, $\delta^{13}C$ in the deep ocean anti-correlates with nutrient concentration. It can thus be used to distinguish the less ventilated and more nutrient rich AABW from the better ventilated and nutrient poor NADW in the modern ocean. The concentration of DIC in AABW and NADW is similar

(~2250 vs. ~2140; (Boyle, 1988; Oppo et al., 2018) and thus the relationship of $\delta^{13}C$ versus % NSW is linear today.

The remineralisation of organic matter in the deep Atlantic mainly reduces reconstructed $\delta^{13}C$. We thus compensated for this effect virtually by increasing the $\delta^{13}C$ values of the observations by a variable degree (Extended Data Table 1). Furthermore, several records from the deep South Atlantic have been hypothesised to be influenced by either the "Mackensen Effect" or a "Habitat Effect" (Gottschalk et al., 2016; Mackensen et al., 1993; Yu et al., 2020) leading to very low glacial $\delta^{13}C$ signatures. We thus incorporated the possibility to compensate for either of these effects individually in the mixing model.

## Stable oxygen isotopes

The stable oxygen isotope signature of water is mainly affected by fractionation through evaporation (favouring $^{16}O$) and precipitation (favouring $^{18}O$). In marine surface waters it is thus determined by net evaporation (increasing $\delta^{18}O$ and salinity) and continental run-off such as river water (decreasing $\delta^{18}O$ and salinity), and hence correlates strongly with salinity. Additionally, sea ice formation in polar regions leads to salinification through brine rejection with insignificant isotopic fractionation (Rasmussen and Thomsen, 2009). Consequently, water that was salinified by brine rejection and which has the same salinity as a reference water that was salinified by evaporation will exhibit lower $\delta^{18}O$ signatures.

Oxygen atoms archived in foraminifera calcite are precipitated from seawater with additional temperature-dependent fractionation (Marchitto et al., 2014; Shackleton, 1974). This leads to $\delta^{18}O$ correlating negatively with precipitation temperature. The combination of both fractionation effects leads to foraminifera calcite $\delta^{18}O$ correlating positively with water density, unless there is a significant contribution of brine-related salinification in the source water (Dokken and Jansen, 1999; Rasmussen and Thomsen, 2009). There are no other processes significantly affecting $\delta^{18}O_b$ in the deep ocean and it is thus a very conservative tracer.

The major challenges of using $\delta^{18}O$ is that its analysis is rather imprecise (analytical uncertainty in terms of single standard deviation is usually around 0.07 ‰) and that uncorrected gas mixing in the mass spectrometer source or other non ideal instrument performance may lead to inter-laboratory offsets of up to 0.30 ‰ (Ostermann and Curry, 2000). Considering that the range of $\delta^{18}O$ in sediment core top benthic foraminifera ($\delta^{18}O_b$) in the Atlantic spans roughly 0.80 ‰ these uncertainties limit the use of $\delta^{18}O$ as a source water tracer today. However, since the range of observed $\delta^{18}O_b$ in the glacial is much larger (> 2 ‰, see Fig. 1), it is actually a valuable tracer for the LGM and HS1.

In the mixing model we therefore did not use $\delta^{18}O_b$ as a source water proxy for the modern or Late Holocene cases, and we corrected $\delta^{18}O_b$ signatures for the two glacial time slices. Since $\delta^{18}O_b$ is precipitated from water molecules, its concentration in source waters is infinite and more importantly exactly equal for all source waters.

## Carbonate ion concentration

Boron concentrations in benthic foraminifera tests correlate linearly with local carbonate ion concentration [$CO_3^{2-}$] in seawater (with species-specific correlation equations; (Yu and Elderfield, 2007). Seawater [$CO_3^{2-}$] in turn depends on seawater pH, alkalinity, and DIC concentrations, and

very little on seawater temperature (Yu et al., 2008). In effect, air-sea $CO_2$ exchange, alkalinity changes in surface waters, and remineralisation of organic matter are the major determinants of source water [$CO_3^{2-}$], and only remineralisation affects subsurface waters (Fig. 2), and in a predictable ratio compared to the changes it induces in $\delta^{13}C$ (Yu et al., 2008).

In the model we corrected for the imprint of organic matter remineralisation on [$CO_3^{2-}$] in the same way as for stable carbon isotopes, applying a conversion factor of 43 µmol/kg per 1‰ change applied to $\delta^{13}C$ following (Yu et al., 2008).

## Radiocarbon ventilation age

Radioactive $^{14}C$ is produced by cosmic rays in the upper atmosphere, mixed into the atmospheric carbon pool, and enters seawater through gas exchange, while it decays radioactively with a half live of about 5.7 ka. Notably, the isotopic equilibration time of radiocarbon between seawater and atmosphere is more than 10 years and thus very long compared to gas exchange times of $CO_2$ in the order of months (Broecker and Peng, 1974). In deep waters, the radiocarbon isotopic signature is only changed by radioactive decay and hence ageing of a water parcel. Here we exclusively consider the differences between calibrated ages from radiocarbon measurements of benthic samples and their actual calendar age, $^{14}C_{b\text{-}atm}$, i.e. the apparent carbon ventilation age.

In the modern Atlantic, actual deep water ageing is less than 500 years (Key et al., 2004; Khatiwala et al., 2012), but could well have been larger during the LGM and in particular during HS1. However, a reasonable implementation of a correction for deep water ageing would require knowledge of advection speeds and pathways, which is beyond the simple mixing model employed here. Considering the large range (400 – 4000 years) and uncertainties (400 – 1000 years; 2 standard errors) in our assigned source water radiocarbon ages we suppose that the effect of ageing within the deep Atlantic is not a dominant control on glacial Atlantic deep water radiocarbon signatures, however, and did not implement it as a specific parametrisation.

## Radiogenic neodymium isotopes

Neodymium is a rare earth element and a trace metal in the environment. It is primarily added to seawater through continental run-off, dissolution of dust in the sea surface, and dissolution of particles in marine sediments. Different rocks carry different radiogenic Nd isotopic signatures (εNd) which are imprinted into source waters by these processes. Dissolved Nd is rather particle reactive and hence adsorbs to sinking particles in the water column while being advected with seawater (Tachikawa et al., 2017).

In the modern Atlantic with its vigorous large scale circulation, advection is fast enough to transport Nd across basins before the effect of sinks and sources becomes dominant, so that it behaves largely conservative in deep waters. However, the sinks and sources may have changed through time, in particular on glacial – interglacial time scales, which can affect the isotopic signatures of source waters as well as the conservativeness of these signatures during water mass advection in the Atlantic (Blaser et al., 2019; Pöppelmeier et al., 2022).

Furthermore, the concentration of Nd in different source waters varies substantially, in the modern analogues to the ones used here roughly by a factor of two from 18 pmol/kg in NAIW to 35 pmol/kg in PDW. There is currently no method of reconstructing past seawater Nd concentrations

directly and the rather complex interplay of sources and sinks make it rather complex to estimate past source water Nd concentrations (Pöppelmeier et al., 2022).

Lastly, the integrity of sedimentary archives of past deep water εNd is still debated and often questionable (Tachikawa et al., 2017). For example, sedimentary authigenic εNd from the Northwest Atlantic and Labrador Sea have been shown to be less radiogenic than local bottom water, apparently due to exchange of Nd with pore waters, which incorporate Nd from partial dissolution of lithogenic sediments (Blaser et al., 2020; Pöppelmeier et al., 2019). But again, it is not certain to which degree these effects occurred in the glacial environment as well.

In the mixing model we incorporate three different parametrisations for the different Nd isotope systematics, in order to simulate the effects of different source water Nd concentrations, fluxes of (unradiogenic) Nd from sediments into SSW within the Atlantic, and biased Northwest Atlantic and Labrador Sea εNd records (see Extended Data Table 1).

## ***Supplementary Text 2:*** Connection between AMW and l-NADW

AMW presents the most important source for lower NADW. Its overflow across the Greenland Scotland Ridge leads to strong entrainment, so that, for example, Denmark Strait Overflow Water exhibits a fractional entrainment factor of 0.55, meaning it is composed of 45 % AMW and 55 % upper NADW and shallow waters entrained into the overflow.

For consistency, we used the source water type definitions of de Carvalho Ferreira and Kerr (2017) for modern and Late Holocene source waters, which comprises l-NADW, but not pure AMW before entrainment. On the other hand, our method of identifying source water signatures in the form of corners in mixing polygons of proxy-proxy plots such as Fig. 1 should yield the signatures of AMW instead of l-NADW, which should lie within the polygon of NADW source waters (assuming u-NADW is the source water that is mostly entrained). For the multi-proxy mixing calculations we thus used l-NADW for the Late Holocene case and glacial AMW for the LGM and HS1 cases. For better comparison we unmixed the Late Holocene l-NADW signal into 55 % u-NADW and 45 % AMW following (Dickson and Brown, 1994) with assigned uncertainties of 5% each in Fig. 3.

The process of source water signature definitions for the glacial time period is associated with significant uncertainties, and it is not entirely clear whether the proxy signatures assigned to AMW should rather be assigned to the already mixed l-NADW. This would make the overall ratio of AMW and u-NADW in the glacial Atlantic more similar to today. Nonetheless, the spatial closeness of carbon and oxygen isotope signatures of AMW-1 and those found in the deep Irminger and Labrador Sea (Fig. 1) suggests that glacial l-NADW contained a larger fraction of AMW than today.

It is important to note that the related uncertainties do not affect the calculations for the overall amount of NADW in the glacial Atlantic, since both AMW and l-NADW are components of NADW. Further multi-proxy studies at individual sites as close as possible to the different source water regions would be necessary in order to better define the different source water proxy signatures and to decipher the connection between u-NADW, l-NADW, and AMW more precisely.

Another interesting feature is that the suggested source water AMW-2 is not actually observed in the glacial proxy data from the Arctic Mediterranean (Fig. 1). This could indicate that AMW-2 did not exist in the way we suggest. For example, the stable isotope signatures trending towards the point where we suggest AMW-2 is located could be formed by mixing u-NADW-2 into a mixture of AMW-1, u-NADW-1, and SSW. Alternatively, AMW-2 could have been formed from AMW-1

within the western subpolar North Atlantic, for example by sea ice brine rejection along the Greenland and Labrador shelves (see also Meland et al., 2008; Seidenkrantz et al., 2021), or subsurface mixing of source waters. Detailed local multi-proxy investigations would be necessary to get more certainty. The effect of removing AMW-2 from the mixing calculations is limited, reducing the average NADW contributions in the deep Atlantic during both the LGM and HS1 from the 74 ± 15 % mentioned in the main text by 7 % (see Extended Data Fig. 3), and affects the results for both time periods equally.

## *Supplementary Text 3:* Descriptions of specific glacial source waters

### Pacific Deep Water

Deep Atlantic SSW today is composed of AABW, whereas in the glacial PDW also spread into the Atlantic (Yu et al., 2020). The proxy signatures between these two SSW are generally more similar than they are to the four NSW, therefore making our a posteriori calculations of SSW and NSW more robust and precise than those for individual source waters (Fig. 3). While the source water attribution to the two SSW types is hence less precise, the mixing model ensemble results do indicate several trends that differentiate these two source waters (Supplementary Fig. 19). For example, in the West Atlantic the ratio of PDW to AABW decreases during their northward advance, meaning that PDW remained more constrained to the South Atlantic. It furthermore appears that AABW was more dense than PDW, which is similar to today and in agreement with (Yu et al., 2020). In the South East Atlantic, i.e. the Cape Basin which is separated from the bulk of the Atlantic by the Wyville Thompson Ridge, AABW was most prevalent below 4 km depth and PDW was layered on top as shallow as 3 km water depth. On the other hand, AABW and PDW were well mixed in the equatorial to subpolar North East Atlantic, probably induced by their passage through constrained fracture zones in the Mid Atlantic Ridge, which is associated with intense mixing. Generally, AABW and PDW were similarly abundant between 48°N and 15°S and the more restricted advance of PDW was probably related to it being less dense and therefore directly competing with l-NADW.

### North Atlantic Bottom Water

It has been hypothesised that the abyssal North Atlantic saw a very dense North Atlantic Bottom Water (NABW) during the LGM (Keigwin and Swift, 2017; Pöppelmeier et al., 2018). These studies were based on sediment core KNR197-10-17GGC from Corner Rise in the northern Northwest Atlantic just South of the Labrador Sea at 5010m water depth. While we did not include a dedicated NABW in our source water ensemble due to the lack of assured observations of this source water, the mixing model analysis does indicate that an AMW-like source water was prevalent and protruded into AABW during the LGM, but much less during HS1 (Extended Data Fig. 9). Potentially, this was a particularly dense mode of AMW that allowed it to sink below AABW.

# Supplementary Tables

***Supplementary Table 1:*** *Number of proxies per site used for the estimation of NADW contributions. Number in brackets indicates proxies with calculated Late Holocene offset to local seawater.*

| # of proxies: | 1 | 2 | 3 | 4 | total sites |
|---|---|---|---|---|---|
| LH | 13 (23) | 48 (40) | 12 (9) | 1 (1) | 74 (73) |
| HS1 | 9 (29) | 61 (28) | 11 (8) | 2 (0) | 83 (65) |
| LGM | 16 (27) | 60 (36) | 16 (9) | 4 (1) | 96 (73) |

***Supplementary Table 2:*** *Number of sites for each proxy used for the estimation of NADW contributions. Number in brackets indicates sites with calculated Late Holocene offset to local seawater.*

| proxies: | $\delta^{13}C$ | $\delta^{18}O$ | $[CO_3^{2-}]$ | εNd | $^{14}C$ |
|---|---|---|---|---|---|
| LH | 62 (62) | 54 (39) | 7 (7) | 19 (19) | 7 (7) |
| HS1 | 73 (48) | 70 (40) | 1 (0) | 15 (15) | 13 (6) |
| LGM | 79 (53) | 71 (43) | 10 (7) | 21 (19) | 19 (8) |

***Supplementary Table*** *3: Estimated source water proxy signature.*

| **source water** | **$\delta^{13}C_b$ (‰)** | **$\delta^{18}O_b$ (‰)** (ivc + oc) | **$[CO_3^{2-}]$ (µmol/kg)** | **εNd** | **$^{14}C_{b\text{-}a}$ age (years)** | **[Nd] (pmol/kg)** | **DIC (µmol/kg)** |
|---|---|---|---|---|---|---|---|
| **modern:** | | | | | | | |
| **AABW** | 0.40 ± 0.05 | 3.20 ± 0.05 | 83 ± 5 | -8.5 ± 0.5 | 1500 ± 150 | 26.5 (1.00) | 2250 (1.00) |
| **u-NADW** | 1.30 ± 0.05 | 2.70 ± 0.10 | 120 ± 5 | -14.2 ± 0.2 | 600 ± 150 | 18.3 (0.69) | 2140 (0.95) |
| **l-NADW** | 1.30 ± 0.05 | 3.25 ± 0.08 | 120 ± 5 | -12.4 ± 0.4 | 1000 ± 150 | 22.8 (0.86) | 2140 (0.95) |
| **glacial:** | | | | | | | |
| **AABW** | -0.83 ± 0.07 | 3.50 ± 0.07 | 87 ± 4 | -6.7 ± 0.4 | 2000 ± 300 | 26.5 (0.76) | 2400 (0.92) |
| **PDW** | -0.40 ± 0.04 | 3.95 ± 0.05 | 50 ± 10 | -3.5 ± 0.3 | 4000 ± 400 | 35.0 (1.00) | 2600 (1.00) |
| **u-NADW-1** | 1.60 ± 0.05 | 3.72 ± 0.09 | 142 ± 8 | -9.5 ± 0.7 | 400 ± 200 | 18.3 (0.52) | 2200 (0.85) |
| **u-NADW-2** | 0.40 ± 0.07 | 2.20 ± 0.21 | 115± 10 | -10.0 ± 1.0 | 2500 ± 500 | 18.3 (0.52) | 2200 (0.85) |
| **AMW-1** | 0.69 ± 0.05 | 4.00 ± 0.07 | 135 ± 20 | -16 ± 1.5 | 400 ± 300 | 22.8 (0.65) | 2200 (0.85) |
| **AMW-2** | 0.03 ± 0.12 | 3.10 ± 0.09 | 135 ± 20 | -16 ± 1.5 | 2500 ± 500 | 22.8 (0.65) | 2200 (0.85) |

Estimated proxy signatures and concentrations of Nd and DIC of all source waters used. Numbers in brackets for concentrations are relative concentrations used in the mixing model.

227

***Supplementary Table** 4: References for source water proxy signatures*

| source water | $\delta^{13}C_b$ | $\delta^{18}O_b$ (‰) | $[CO_3^{2-}]$ | εNd | $^{14}C_{b\text{-}a}$ age |
|---|---|---|---|---|---|
| **modern:** | | | | | |
| **AABW** | Yu et al. (2020) | Hoffman & Lund (2012) | Yu et al. (2020) | Yu et al. (2020) | Skinner et al. (2017) |
| **u-NADW** | Yu et al. (2020) | Hoffman & Lund (2012) | Yu et al. (2020) | Van de Flierdt et al. (2016) | Skinner et al. (2017) and seawater data |
| **l-NADW** | Yu et al. (2020) | Hoffman & Lund (2012) | Yu et al. (2020) | Lambelet et al. (2016) | Skinner et al. (2017) and seawater data |
| **glacial:** | | | | | |
| **AABW** | Yu et al. (2020), Curry and Oppo (2005) and data trend at SE – SW > 4 km depth | data trend at SE – SW Atlantic > 4 km depth | Yu et al. (2020) and data trend at SE – SW 4-6 km depth | Yu et al. (2020) and data trend at SE - SW 4-6 km depth, modern concentrations | SW and SE abyssal data |
| **PDW** | Yu et al. (2020) and data trend at SE – SW 3-4 km depth | data trend at SE - SW Atlantic 3-4 km depth | Yu et al. (2020) and data trend at SE - SW 3-4 km depth | Yu et al. (2020) and data trend at SE – SW 3-4 km depth, concentrations related to LGM eNd offset from modern | Skinner et al. (2017), Pacific data |
| **u-NADW-1** | Oppo et al. (2015), SPE data | Oppo et al. (2015), SPE data | Yu et al. (2008), SPE data | Zhao et al. (2019) NW eNd data & Roberts & Piotrowski (2015) SPE eNd data, modern concentrations | Thornalley et al. (2011) Iceland Ridge data |
| **u-NADW-2** | Oppo et al. (2015), SPE data | Oppo et al. (2015), SPE data | Yu et al. (2008) SPE data | Zhao et al. (2019) NW eNd data & Roberts & Piotrowski (2015) SPE eNd data, modern concentrations | Thornalley et al. (2011) Iceland Ridge data |
| **AMW** | Altuna et al. (2021 ) Arctic Mediterranean data | Altuna et al. (2021) Arctic Mediterranean data | Yu et al. (2008) SPE data | Blaser et al. (2020), modern concentrations | assumed similar to glacial NAIW |
| **AMW-2** | this study Arctic & SPW | this study Arctic & SPW | Yu et al. (2008) SPE data | Blaser et al. (2020), modern concentrations | assumed similar to glacial b-NAIW |

***Supplementary Table 5:** Regional salinity - oxygen isotope signature regressions from seawater. S = salinity in PSU. Equations yield seawater $\delta^{18}O$ vs. VSMOW in ‰.*

| basin | water depth | equation |
|---|---|---|
| North Atlantic | < 2000 m | 0.766 * S - 26.549 |
| North Atlantic | >= 2000 m | 1.409 * S - 48.950 |
| South Atlantic | < 2000 m | 0.488 * S - 16.859 |
| South Atlantic | >= 2000 m | 1.572 * S - 54.649 |
| Pacific | all | 0.4385 * S - 15.1851 |
| Arctic Mediterranean | < 1500 m | 0.3654 * S - 12.485 |

228

***Supplementary Table 6 (separate csv file):** Description of column headers and full references used in Suplementary Tables 7 – 10.*

***Supplementary Table 7 (separate csv file):** New carbon and oxygen stable isotope data record from Site IODP U1302.*

***Supplementary Table 8 (separate csv file):** Carbon and oxygen stable isotope data used for Fig. 1.*

***Supplementary Table 9 (separate csv file):*** *Summary of sediment core sites including number of available data for each of the five proxies used.*

***Supplementary Table 10 (separate csv file):*** *Full time period averaged proxy data set used for the mixing model calculations.*

229

# Supplementary Figures

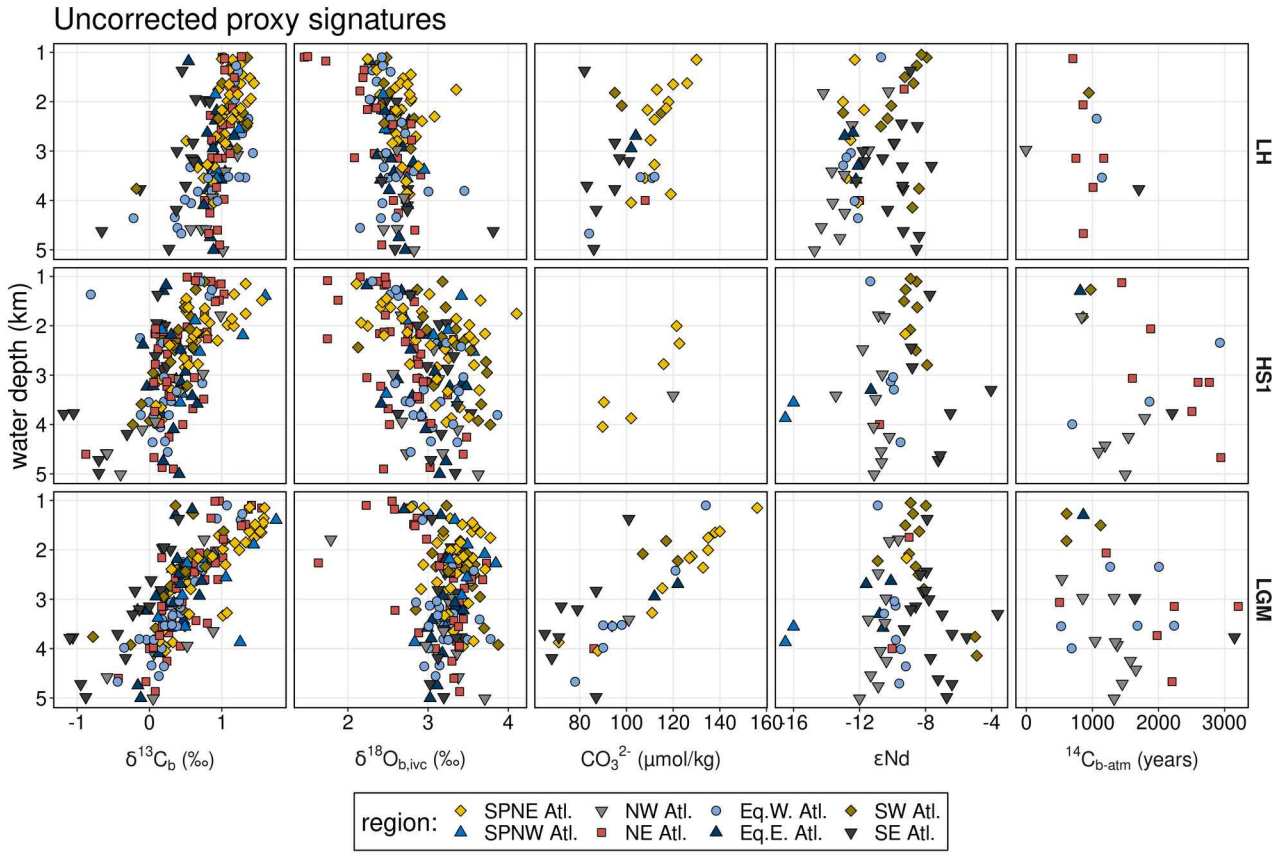


***Supplementary Fig. 1:*** *Compiled proxy data from LH, HS1, and LGM. Symbols code the regions where the sediment sites are located. Note that only data in the equatorial and North Atlantic below 2 km water depth were used for the estimation of NADW abundance. SPN = subpolar North Atlantic*

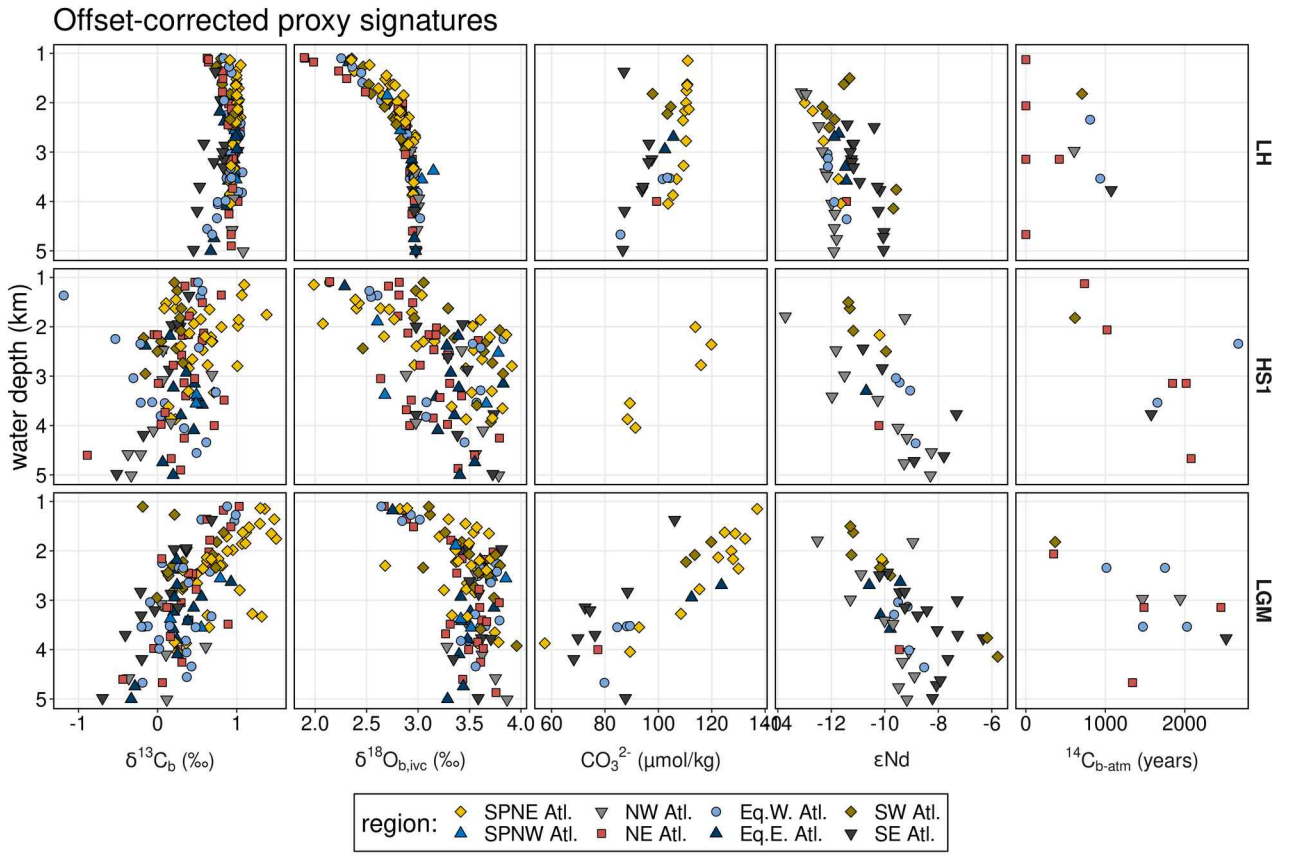


233

***Supplementary Fig. 2:*** *Compiled proxy data from LH, HS1, and LGM, corrected for Late Holocene to seawater offsets. Data with large corrections, i.e. within the grey shaded areas in Supplementary Fig. 3 are not shown. Symbols code the regions where the sediment sites are located. SPN = subpolar North Atlantic*

234

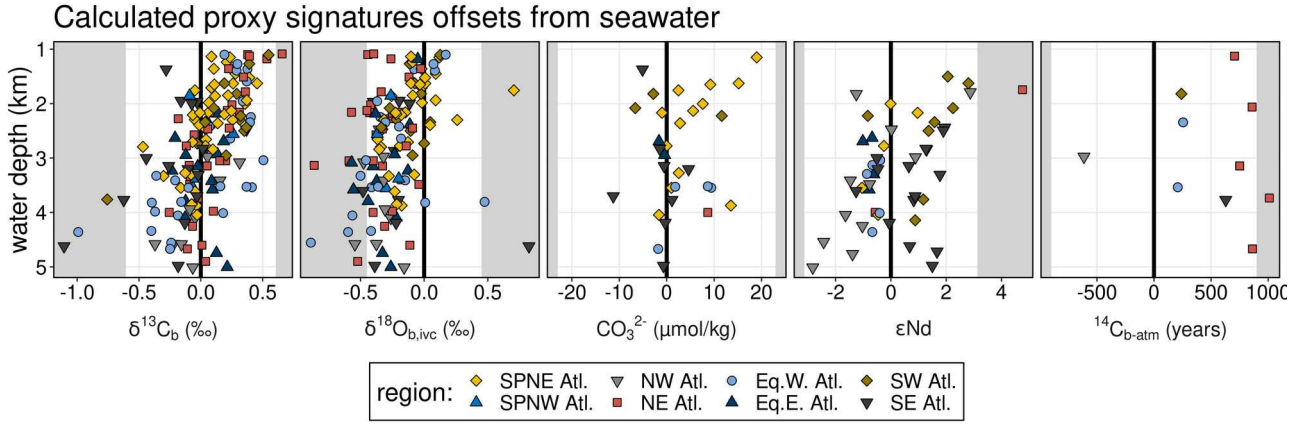


235

***Supplementary Fig. 3:*** *Proxy data Late Holocene to seawater offsets. Symbols code the regions where the sediment sites are located. Grey shaded areas indicate offsets that are more than 25% of the respective proxy range in the source water compositions. Data within the grey areas were discarded for model runs with offset correction.*

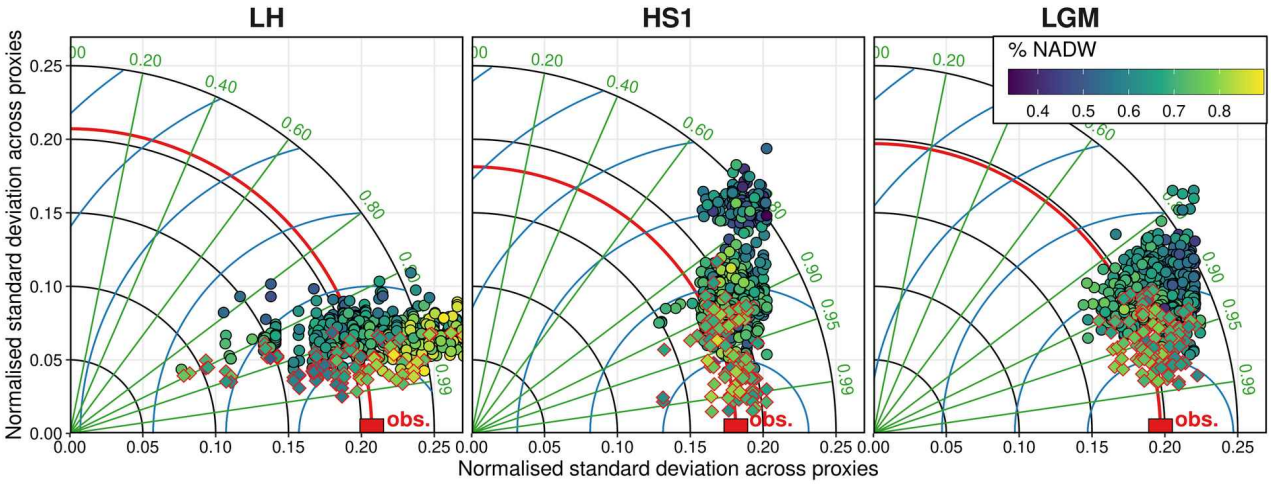


236

***Supplementary Fig. 4:*** *Taylor diagrams showing summary statistics of the different mixing model runs. Taylor diagrams show how closely the gross pattern of the modelled data match the pattern of the observations (red square; . The distance from origin (black circles) indicates the relative standard deviation of the model results, green radial lines indicate correlation coefficient between observations and model results, blue circles centred on observations indicate root mean square error among observations and model results. The closer a simulation lies to the observations the better its pattern matches with those of the observations. The point colour indicates the amount of NADW in this specific model run. Red-bordered diamond symbols are the 10% of ensemble results with the lowest cost function (see Methods).*

237

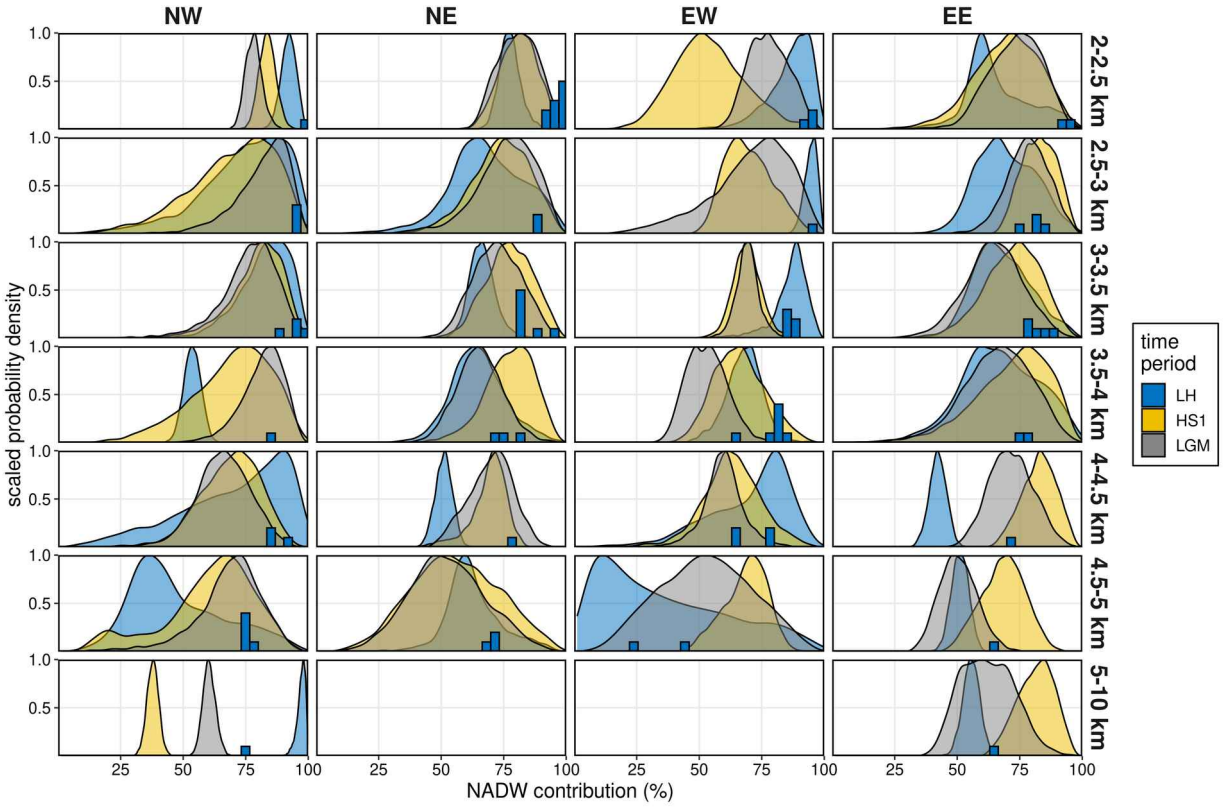


238

***Supplementary Fig. 5:*** Example output of the mixing model. Shown are probability densities of NADW contribution for all three time slices in all model boxes used for the estimation of deep Atlantic NADW abundance for the "base" model runs without any modifications. Blue bars are histograms (top of each panel equals 10 observations) of modern seawater NADW contributions estimated at the locations where Late Holocene sediment observations exist.

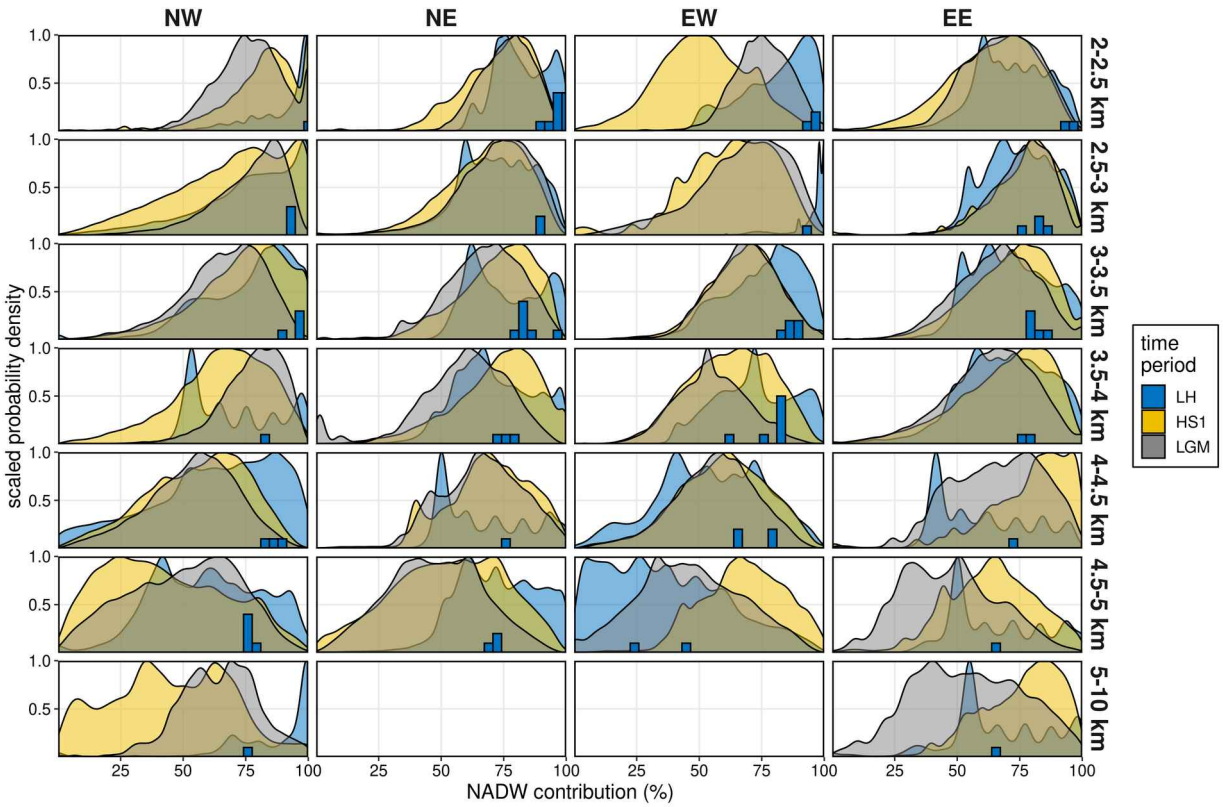


***Supplementary Fig. 6:*** Example output of the mixing model ensemble. Same as Supplementary Fig. 5 but with probability densities aggregated across the whole mixing model ensemble.

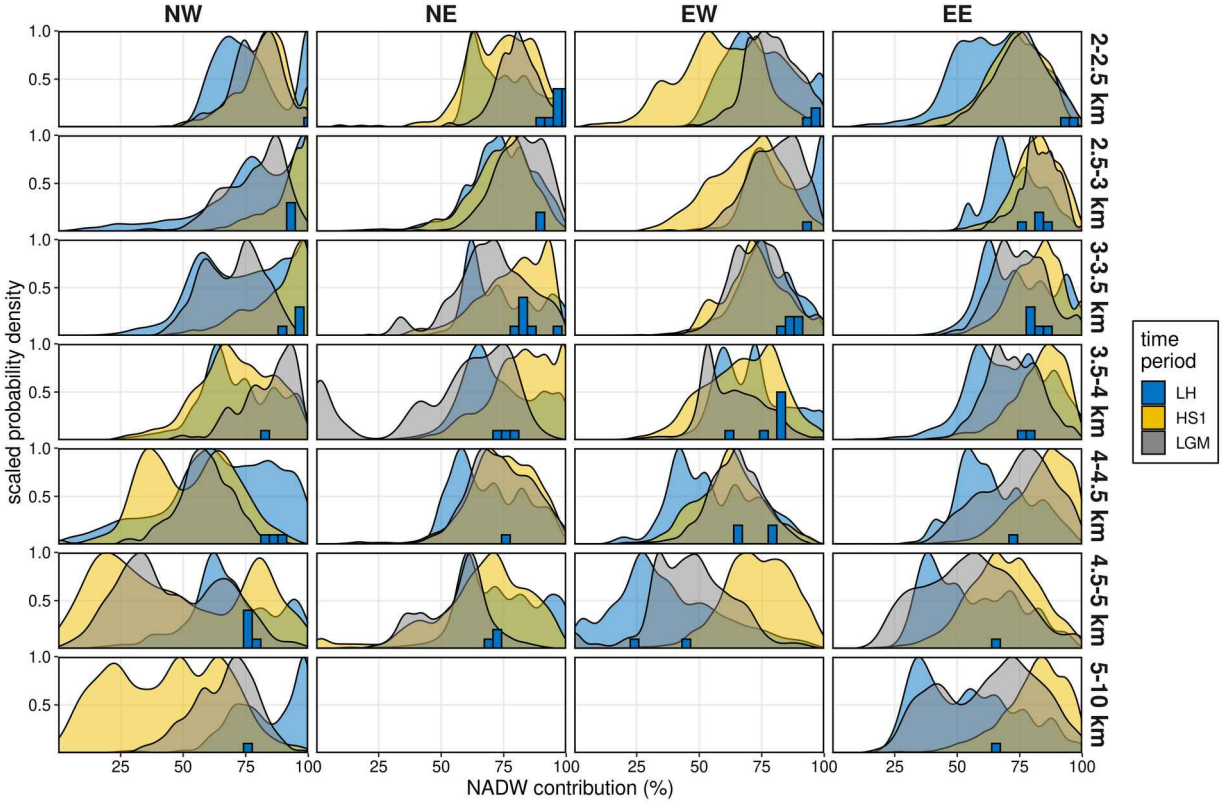


***Supplementary Fig. 7:*** Example output of the best 10% of mixing model ensemble. Same as Supplementary Fig. 5 but with probability densities aggregated across the best 10% of runs of the mixing model ensemble (assessed with the cost function described in the methods, see also Supplementary Fig. 4).

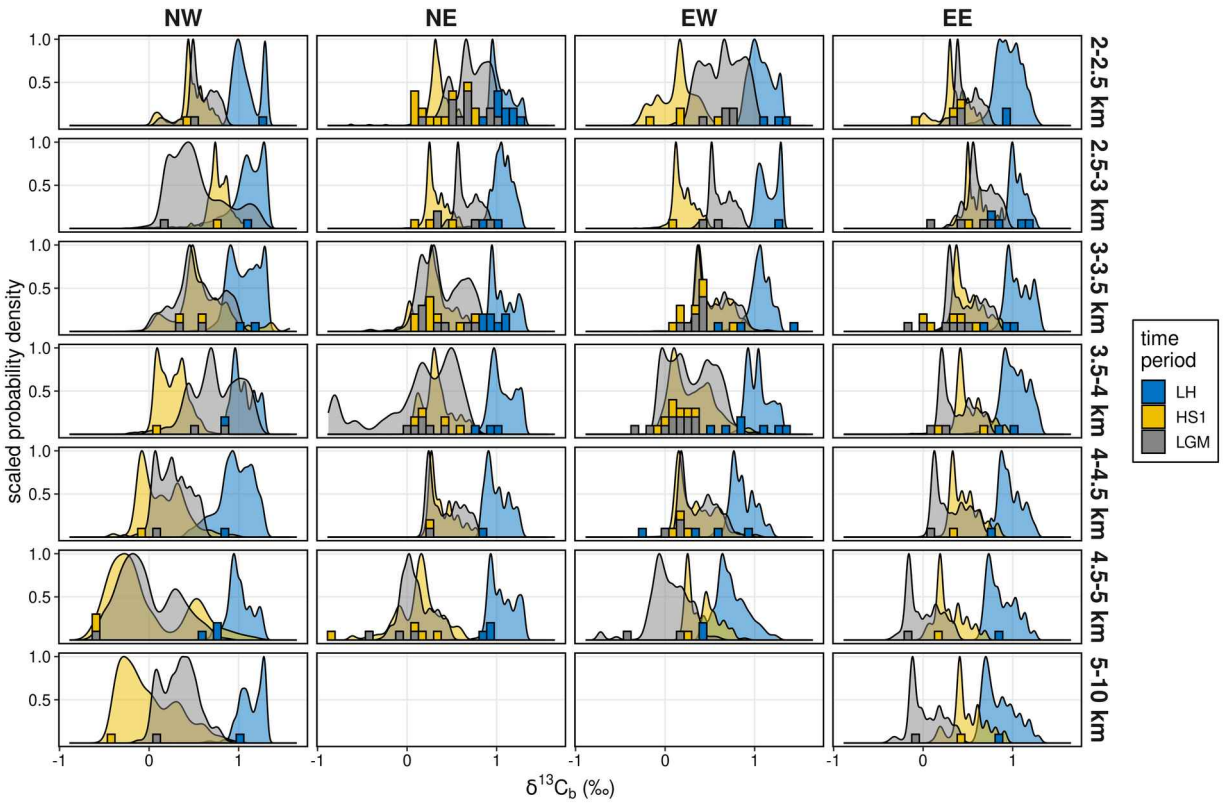


***Supplementary Fig. 8:*** Example output of $\delta^{13}C_b$ data from the mixing model ensemble. Same as Supplementary Fig. 7 but x-axes show $\delta^{13}C_b$ modelled (probability density curves) and observed (histograms).

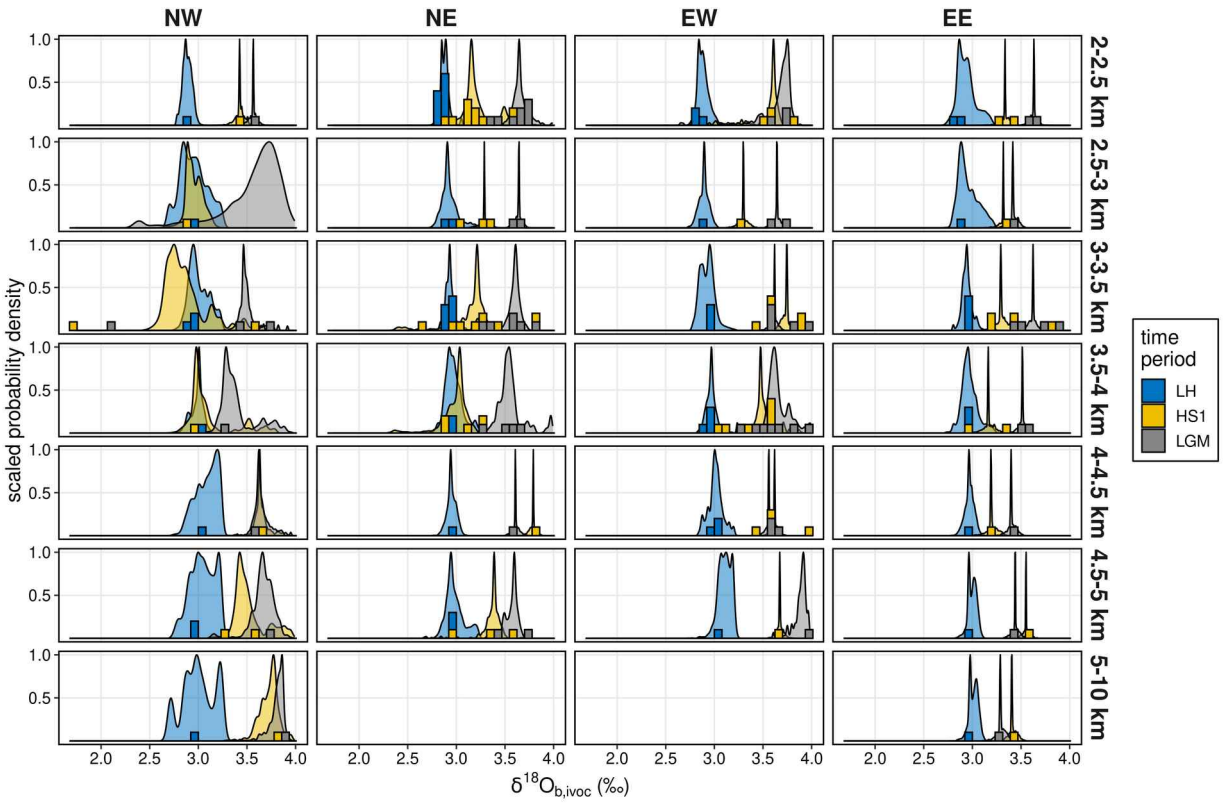


242

***Supplementary Fig. 9:*** Example output of $\delta^{18}O_{b,\,ivoc}$ data from the mixing model ensemble. Same as Supplementary Fig. 7 but x-axes show $\delta^{18}O_{b,\,ivoc}$ modelled (probability density curves) and observed (histograms).

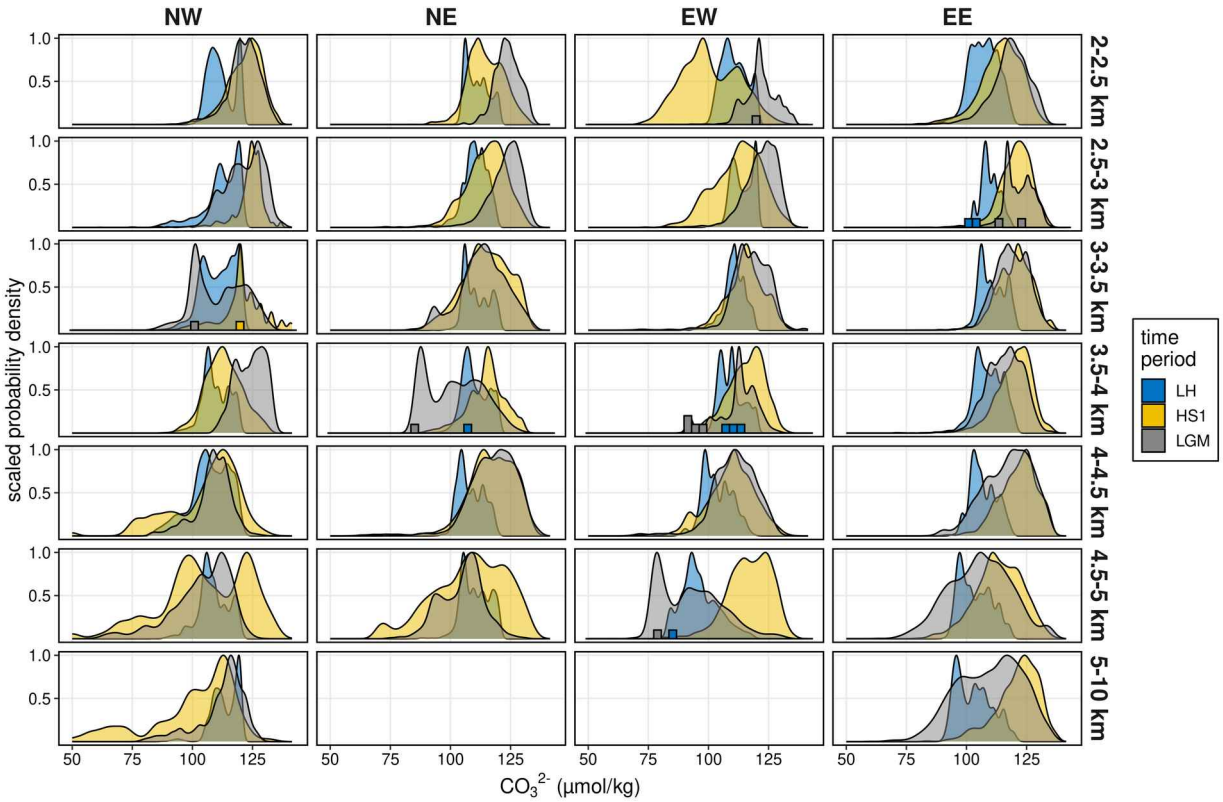


243

***Supplementary Fig. 10:*** Example output of $[CO_3^{2-}]$ data from the mixing model ensemble. Same as Supplementary Fig. 7 but x-axes show $[CO_3^{2-}]$ modelled (probability density curves) and observed (histograms).

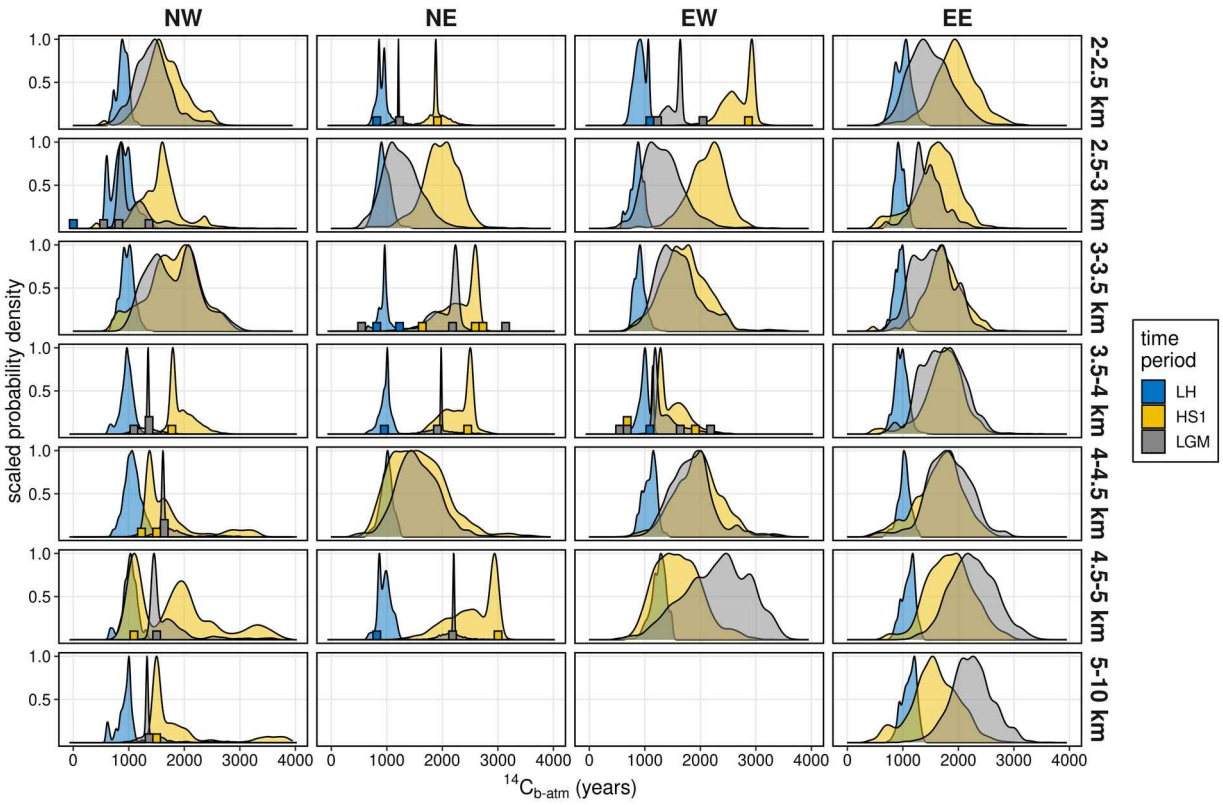


244

***Supplementary Fig. 11:*** Example output of $^{14}C_{b\text{-}atm}$ data from the mixing model ensemble. Same as Supplementary Fig. 7 but x-axes show $^{14}C_{b\text{-}atm}$ modelled (probability density curves) and observed (histograms).

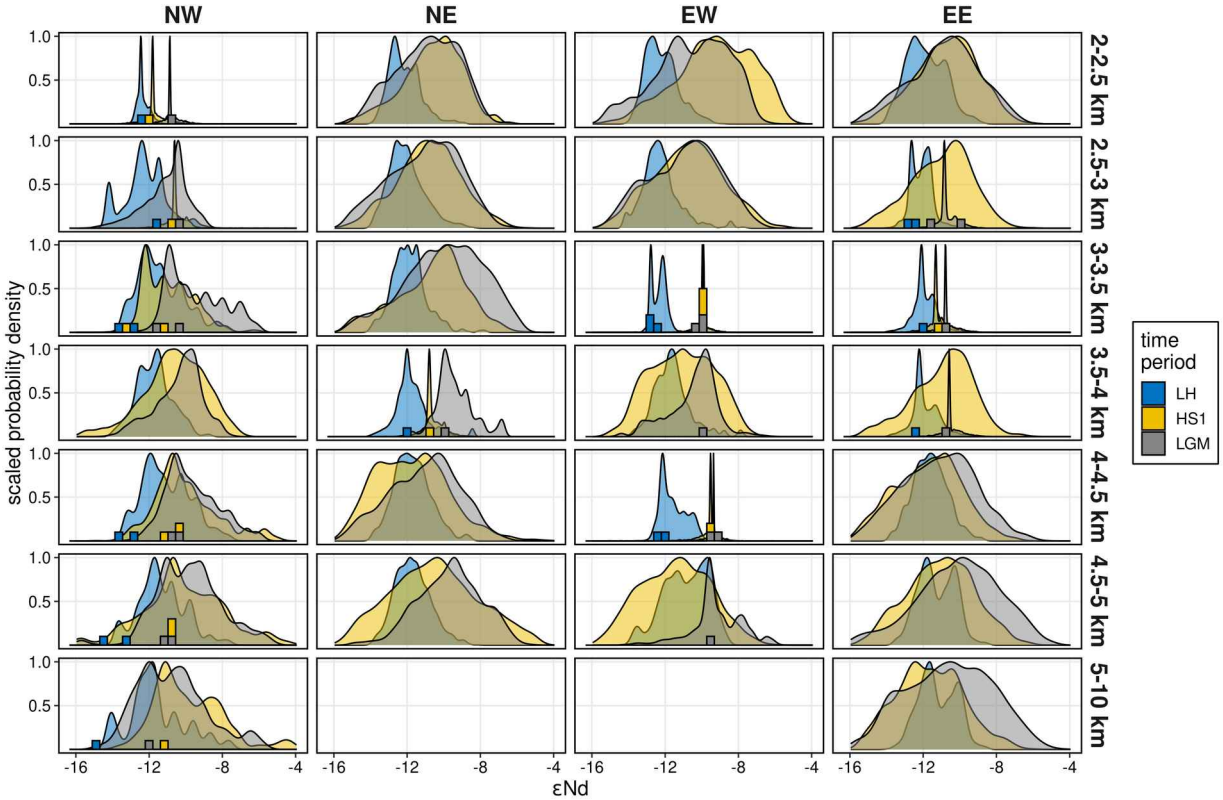


245

***Supplementary Fig. 12:*** Example output of εNd data from the mixing model ensemble. Same as Supplementary Fig. 7 but x-axes show εNd modelled (probability density curves) and observed (histograms).

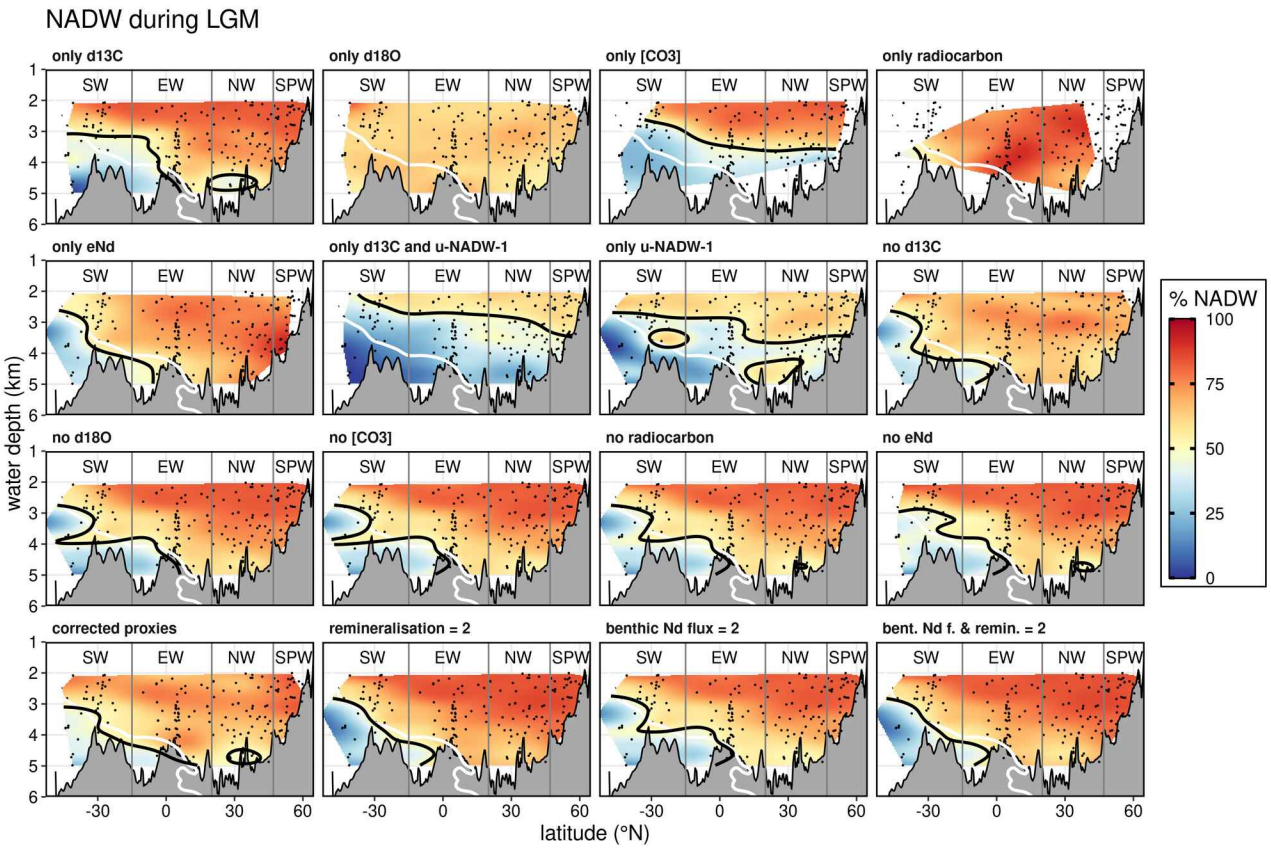


246

***Supplementary Fig. 13:*** *Bulk NADW contributions during the LGM along a West Atlantic Transect. Here, for better visualisation NADW contributions were calculated for each site instead of aggregating them in boxes, and then smoothed on a 2D surface along the GEOSECS transect. Each panel depicts the result of one model run (numbers in run names indicate the strength x of the respective non-conservative effect parametrisation, see Extended Data Table 1), colour indicates the contribution of NADW, black line is the 50 % contour, and white line is the 50% contour from modern seawater data (de Carvalho Ferreira and Kerr, 2017; Taylor, 2001). Vertical lines separate model regions (see Extended Data Fig. 1), of which only the equatorial and northern regions were used for the mixing model ensemble. Note that these section plots are only meant for visualisation and do not directly reflect the output of the mixing model runs, where proxy data were aggregated within model boxes, thereby combining proxies directly before calculations.*

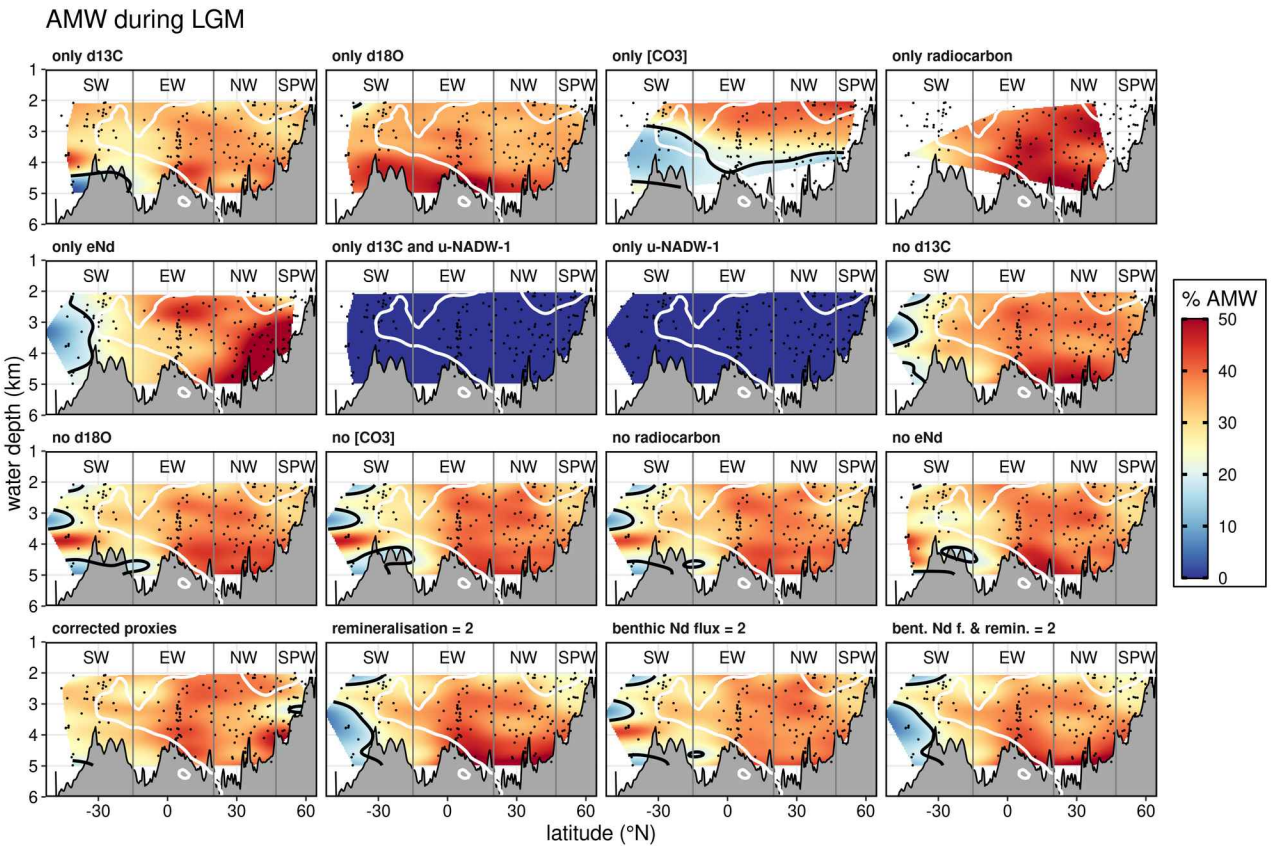


247

***Supplementary Fig. 14:*** *Same as Supplementary Fig. 13, but for bulk AMW. Black and white contours indicate 20 % AMW in the model runs and in modern seawater, respectively. Note that the colour scale was capped at 50 %.*

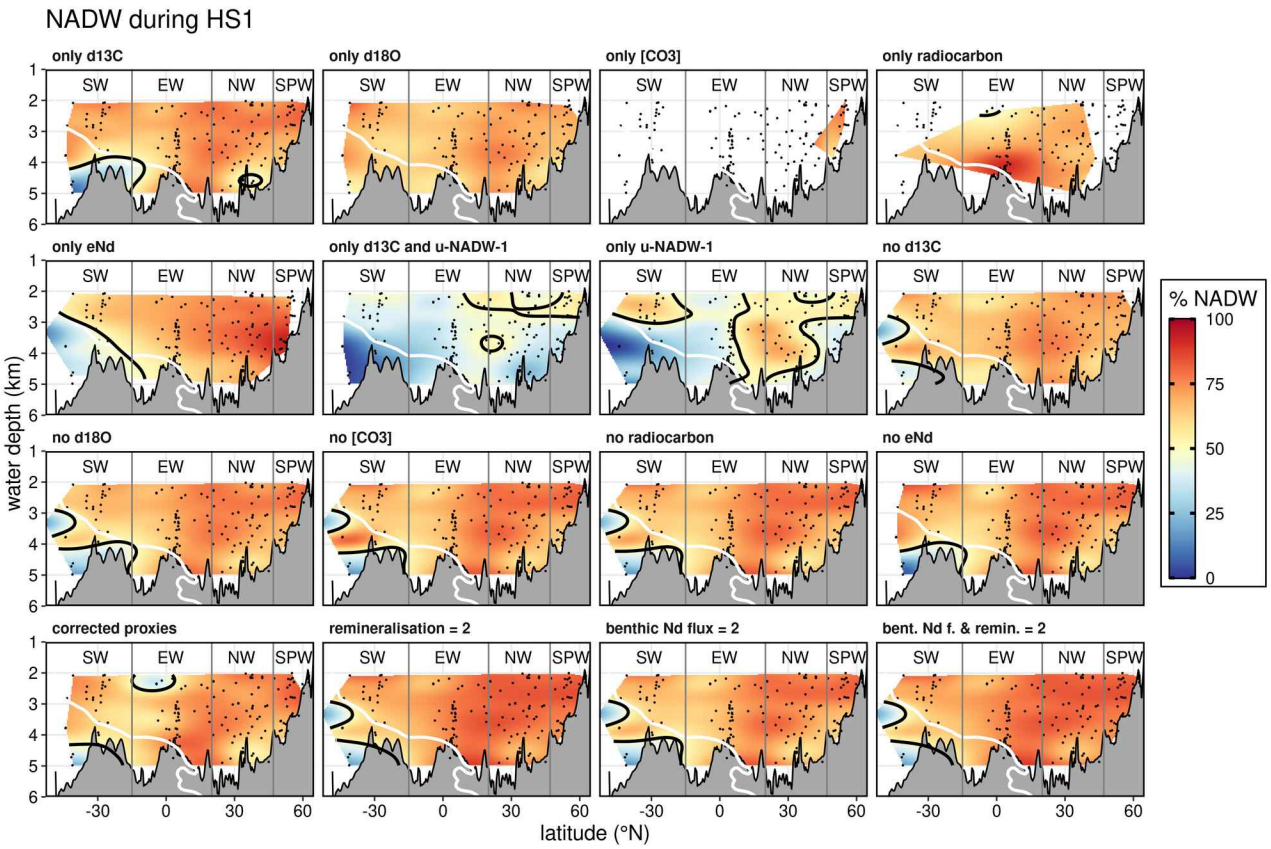


248

***Supplementary Fig. 15:*** *Same as Supplementary Fig. 13, but for HS1.*

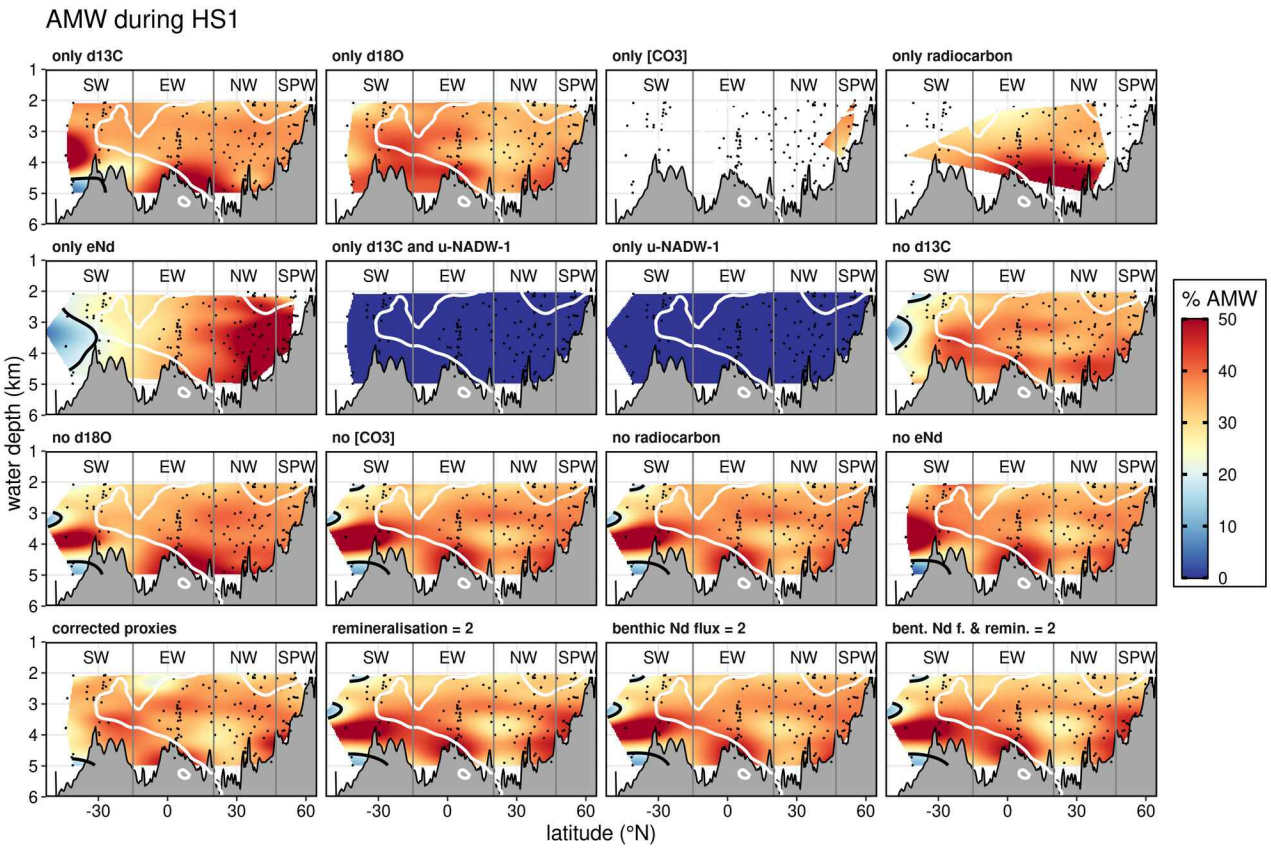


249

***Supplementary Fig. 16:*** *Same as Supplementary Fig. 14, but for HS1.*

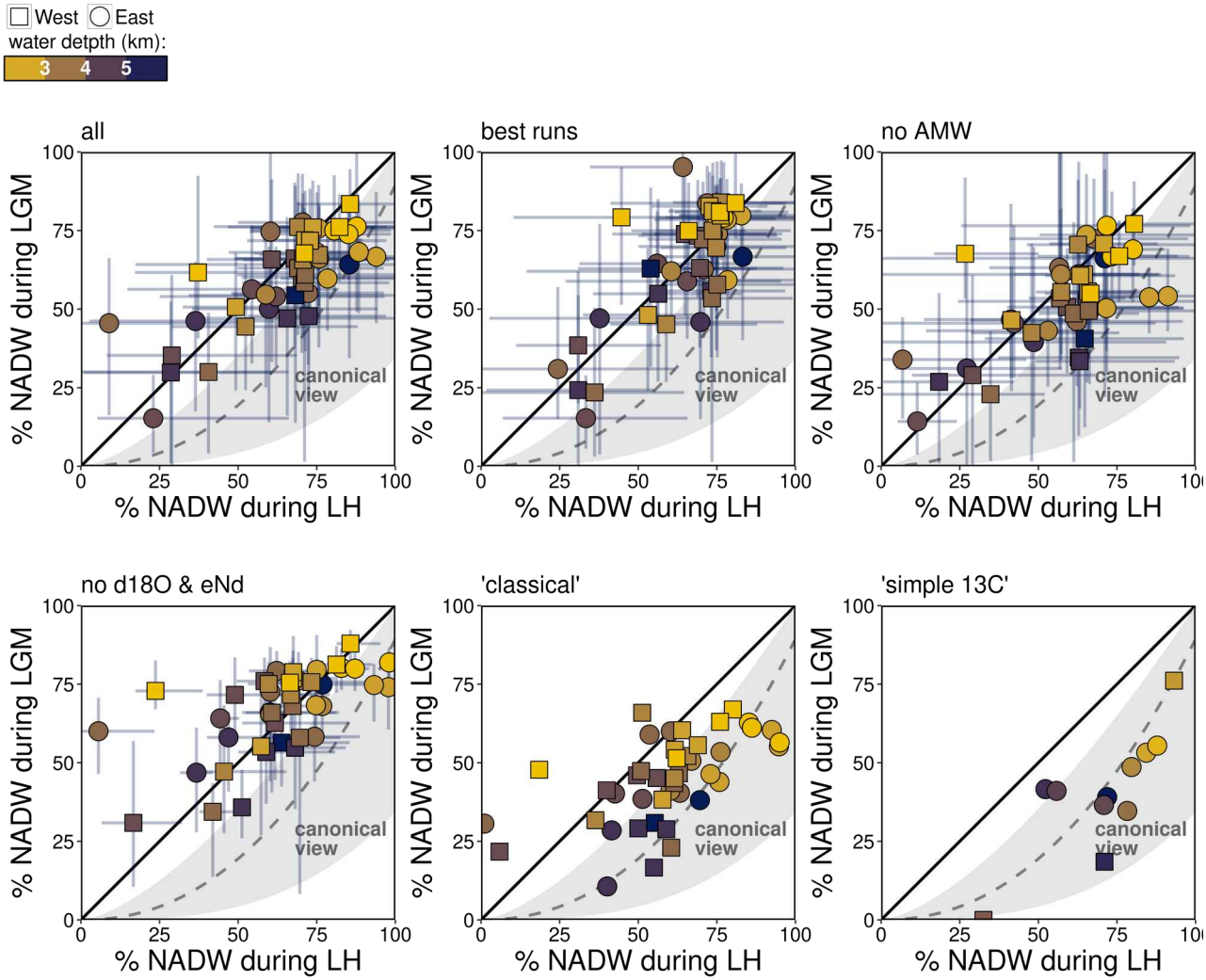


250

***Supplementary Fig. 17:*** *Comparisons of bulk NADW contributions from LGM and LH. Each panel shows a different subset of the simmr ensemble and two cases using only $\delta^{13}C_b$ as proxy and AABW and u-NADW-1 source waters ("classical" as simmr-based calculation and "simple 13C" as simple linear mixing calculation). "best runs" denotes the 10% ensemble runs with the best performance (see Methods and Supplementary Fig. 4). Symbols, lines, and shading like in Fig. 4.*

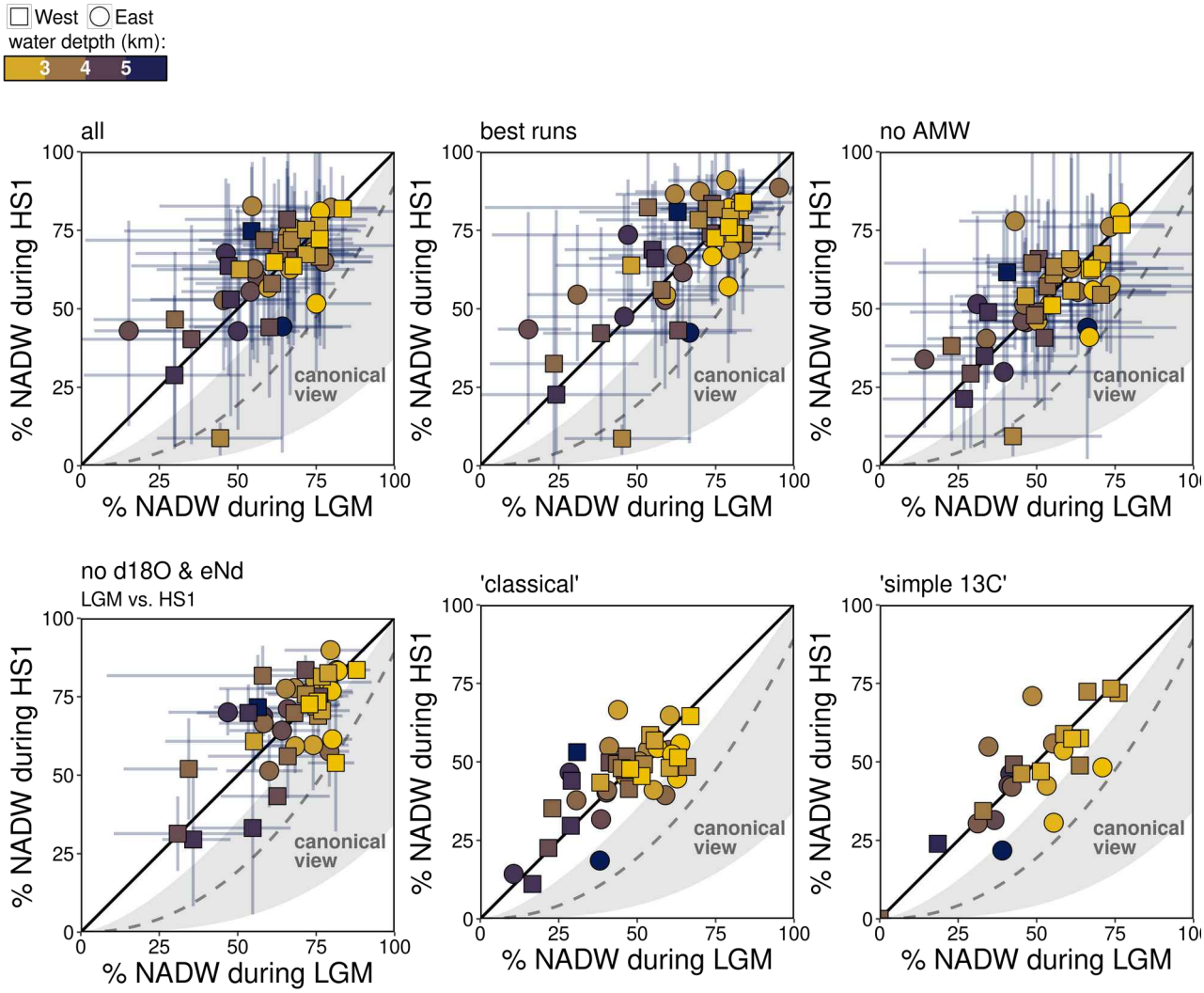


***Supplementary Fig. 18:*** *Comparisons of bulk NADW contributions from HS1 and LGM. Each panel shows a different subset of the simmr ensemble and two cases using only $\delta^{13}C_b$ as proxy and AABW and u-NADW-1 source waters ("classical" as simmr-based calculation and "simple 13C" as simple linear mixing calculation). "best runs" denotes the 10% ensemble runs with the best performance (see Methods and Supplementary Fig. 4). Symbols, lines, and shading like in Fig. 4.*

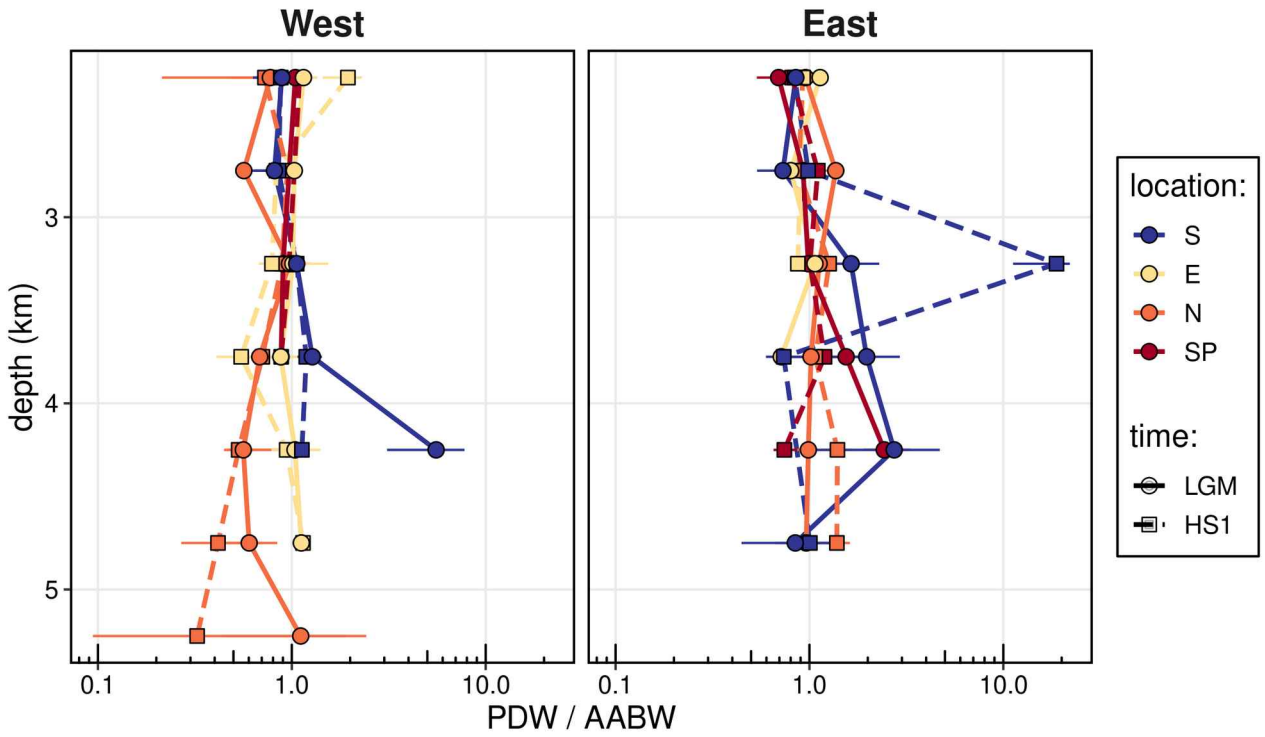


252

***Supplementary Fig. 19:*** *Depth trends of the ratio of PDW vs. AABW across model ensemble for different regions during the LGM and HS1. Colours indicate latitudinal boxes (South, Equatorial, North, and Subpolar North, combining the eastern and western boxes of Extended Data Fig. 1) and panels differentiate West and East Atlantic basins. Points and error bars indicate medians and central 50% of data.*

253 # References used in this document


Blaser, P., Gutjahr, M., Pöppelmeier, F., Frank, M., Kaboth-Bahr, S., Lippold, J., 2020. Labrador Sea bottom water provenance and REE exchange during the past 35,000 years. Earth and Planetary Science Letters 542, 116299. https://doi.org/10.1016/j.epsl.2020.116299

Blaser, P., Pöppelmeier, F., Schulz, H., Gutjahr, M., Frank, M., Lippold, J., Heinrich, H., Link, J.M., Hoffmann, J., Szidat, S., Frank, N., 2019. The resilience and sensitivity of Northeast Atlantic deep water εNd to overprinting by detrital fluxes over the past 30,000 years. Geochimica et Cosmochimica Acta 245, 79–97. https://doi.org/10.1016/j.gca.2018.10.018

Boyle, E.A., 1988. Cadmium: Chemical tracer of deepwater paleoceanography. Paleoceanography 3, 471–489. https://doi.org/10.1029/PA003i004p00471

Broecker, W.S., Peng, T.-H., 1974. Gas exchange rates between air and sea. Tellus 26, 21–35. https://doi.org/10.3402/tellusa.v26i1-2.9733

de Carvalho Ferreira, M.L., Kerr, R., 2017. Source water distribution and quantification of North Atlantic Deep Water and Antarctic Bottom Water in the Atlantic Ocean. Progress in Oceanography 153, 66–83. https://doi.org/10.1016/j.pocean.2017.04.003

Dickson, R.R., Brown, J., 1994. The production of North Atlantic Deep Water: Sources, rates, and pathways. Journal of Geophysical Research: Oceans 99, 12319–12341. https://doi.org/10.1029/94JC00530

Dokken, T.M., Jansen, E., 1999. Rapid changes in the mechanism of ocean convection during the last glacial period. Nature 401, 458–461. https://doi.org/10.1038/46753

Duplessy, J.-C., Shackleton, N.J., Matthews, R.K., Prell, W., Ruddiman, W.F., Caralp, M., Hendy, C.H., 1984. 13C Record of benthic foraminifera in the last interglacial ocean: Implications for the carbon cycle and the global deep water circulation. Quaternary Research 21, 225–243. https://doi.org/10.1016/0033-5894(84)90099-1

Gottschalk, J., Vázquez Riveiros, N., Waelbroeck, C., Skinner, L.C., Michel, E., Duplessy, J.-C., Hodell, D., Mackensen, A., 2016. Carbon isotope offsets between benthic foraminifer species of the genus Cibicides (Cibicidoides) in the glacial sub-Antarctic Atlantic. Paleoceanography 31, 2016PA003029. https://doi.org/10.1002/2016PA003029

Keigwin, L.D., Swift, S.A., 2017. Carbon isotope evidence for a northern source of deep water in the glacial western North Atlantic. Proceedings of the National Academy of Sciences 114, 2831–2835. https://doi.org/10.1073/pnas.1614693114

Key, R.M., Kozyr, A., Sabine, C.L., Lee, K., Wanninkhof, R., Bullister, J.L., Feely, R.A., Millero, F.J., Mordy, C., Peng, T.-H., 2004. A global ocean carbon climatology: Results from Global Data Analysis Project (GLODAP). Global Biogeochemical Cycles 18. https://doi.org/10.1029/2004GB002247

Khatiwala, S., Primeau, F., Holzer, M., 2012. Ventilation of the deep ocean constrained with tracer observations and implications for radiocarbon estimates of ideal mean age. Earth and Planetary Science Letters 325–326, 116–125. https://doi.org/10.1016/j.epsl.2012.01.038

Mackensen, A., Hubberten, H.-W., Bickert, T., Fischer, G., Fütterer, D.K., 1993. The δ13C in benthic foraminiferal tests of Fontbotia wuellerstorfi (Schwager) Relative to the δ13C of dissolved inorganic carbon in Southern Ocean Deep Water: Implications for glacial ocean circulation models. Paleoceanography 8, 587–610. https://doi.org/10.1029/93PA01291

Marchitto, T.M., Curry, W.B., Lynch-Stieglitz, J., Bryan, S.P., Cobb, K.M., Lund, D.C., 2014. Improved oxygen isotope temperature calibrations for cosmopolitan benthic foraminifera. Geochimica et Cosmochimica Acta 130, 1–11. https://doi.org/10.1016/j.gca.2013.12.034

Meland, M.Y., Dokken, T.M., Jansen, E., Hevrøy, K., 2008. Water mass properties and exchange between the Nordic seas and the northern North Atlantic during the period 23-6 ka: Benthic oxygen isotopic evidence. Paleoceanography 23. https://doi.org/10.1029/2007PA001416

Oppo, D.W., Gebbie, G., Huang, K.-F., Curry, W.B., Marchitto, T.M., Pietro, K.R., 2018. Data Constraints on Glacial Atlantic Water Mass Geometry and Properties. Paleoceanography and Paleoclimatology 33, 1013–1034. https://doi.org/10.1029/2018PA003408

Ostermann, D.R., Curry, W.B., 2000. Calibration of stable isotopic data: An enriched δ18O standard used for source gas mixing detection and correction. Paleoceanography 15, 353–360. https://doi.org/10.1029/1999PA000411

Pöppelmeier, F., Blaser, P., Gutjahr, M., Süfke, F., Thornalley, D.J.R., Grützner, J., Jakob, K.A., Link, J.M., Szidat, S., Lippold, J., 2019. Influence of Ocean Circulation and Benthic Exchange on Deep Northwest Atlantic Nd Isotope Records During the Past 30,000 Years. Geochemistry, Geophysics, Geosystems 20, 4457–4469. https://doi.org/10.1029/2019GC008271

Pöppelmeier, F., Gutjahr, M., Blaser, P., Keigwin, L.D., Lippold, J., 2018. Origin of Abyssal NW Atlantic Water Masses Since the Last Glacial Maximum. Paleoceanography and Paleoclimatology 33, 530–543. https://doi.org/10.1029/2017PA003290

Pöppelmeier, F., Lippold, J., Blaser, P., Gutjahr, M., Frank, M., Stocker, T.F., 2022. Neodymium isotopes as a paleo-water mass tracer: A model-data reassessment. Quaternary Science Reviews 279, 107404. https://doi.org/10.1016/j.quascirev.2022.107404

Rasmussen, T.L., Thomsen, E., 2009. Stable isotope signals from brines in the Barents Sea: Implications for brine formation during the last glaciation. Geology 37, 903–906. https://doi.org/10.1130/G25543A.1

Schmittner, A., Bostock, H.C., Cartapanis, O., Curry, W.B., Filipsson, H.L., Galbraith, E.D., Gottschalk, J., Herguera, J.C., Hoogakker, B., Jaccard, S.L., Lisiecki, L.E., Lund, D.C., Martínez-Méndez, G., Lynch-Stieglitz, J., Mackensen, A., Michel, E., Mix, A.C., Oppo, D.W., Peterson, C.D., Repschläger, J., Sikes, E.L., Spero, H.J., Waelbroeck, C., 2017. Calibration of the carbon isotope composition ($\delta^{13}C$) of benthic foraminifera. Paleoceanography 32, 512–530. https://doi.org/10.1002/2016PA003072

Seidenkrantz, M.-S., Kuijpers, A., Aagaard-Sørensen, S., Lindgreen, H., Olsen, J., Pearce, C., 2021. Evidence for influx of Atlantic water masses to the Labrador Sea during the Last Glacial Maximum. Scientific Reports 11, 6788. https://doi.org/10.1038/s41598-021-86224-z

Shackleton, N.J., 1974. Attainment of isotopic equilibrium between ocean water and benthonic foraminifera genus Uvigerina : isotopic changes in the ocean during the last glacial, in: Les Méthodes Quantitatives D'Etude Des Variations Du Climat Au Cours Du Pléistocène, 209. Presented at the Colloques Internationaux du C.N.R.S., Gif-sur-Yvette, p. 203.

Tachikawa, K., Arsouze, T., Bayon, G., Bory, A., Colin, C., Dutay, J.-C., Frank, N., Giraud, X., Gourlan, A.T., Jeandel, C., Lacan, F., Meynadier, L., Montagna, P., Piotrowski, A.M., Plancherel, Y., Pucéat, E., Roy-Barman, M., Waelbroeck, C., 2017. The large-scale evolution of neodymium isotopic composition in the global modern and Holocene ocean revealed from seawater and archive data. Chemical Geology 457, 131–148. https://doi.org/10.1016/j.chemgeo.2017.03.018

Taylor, K.E., 2001. Summarizing multiple aspects of model performance in a single diagram. Journal of Geophysical Research: Atmospheres 106, 7183–7192. https://doi.org/10.1029/2000JD900719

Yu, J., Elderfield, H., 2007. Benthic foraminiferal B/Ca ratios reflect deep water carbonate saturation state. Earth and Planetary Science Letters 258, 73–86. https://doi.org/10.1016/j.epsl.2007.03.025

Yu, J., Elderfield, H., Piotrowski, A.M., 2008. Seawater carbonate ion-δ13C systematics and application to glacial–interglacial North Atlantic ocean circulation. Earth and Planetary Science Letters 271, 209–220. https://doi.org/10.1016/j.epsl.2008.04.010

Yu, J., Menviel, L., Jin, Z.D., Anderson, R.F., Jian, Z., Piotrowski, A.M., Ma, X., Rohling, E.J., Zhang, F., Marino, G., McManus, J.F., 2020. Last glacial atmospheric CO 2 decline due to widespread Pacific deep-water expansion. Nature Geoscience 1–6. https://doi.org/10.1038/s41561-020-0610-5